# An overview of hydroxy-based polyanionic cathode insertion materials for metal-ion batteries

Shashwat Singh, Shubham Lochab, Lalit Sharma, Valérie Pralong, Prabeer Barpanda

PCCP

# An overview of hydroxy-based polyanionic cathode insertion materials for metal-ion batteries

| | |
|---|---|
| Journal: | *Physical Chemistry Chemical Physics* |
| Manuscript ID | Draft |
| Article Type: | Perspective |
| Date Submitted by the Author: | n/a |
| Complete List of Authors: | Singh, Shashwat; Indian Institute of Science, Materials Researh Center<br>Lohchab, Shubham; Indian Institute of Science, Materials Researh Center<br>Sharma, Lalit; Indian Institute of Science, Materials Researh Center<br>Pralong, Valerie; CNRS, Chemistry<br>Barpanda, Prabeer; Indian Institute of Science, Materials Researh Center |
| | |

**Perspective** Manuscript for **Phys Chem Chem Phys.**

# An overview of hydroxy-based polyanionic cathode insertion materials for metal-ion batteries

Shashwat Singh,[a§] Shubham Lochab,[a,b§] Lalit Sharma,[a,c]
Valérie Pralong,[d] and Prabeer Barpanda[a] *

*a. Faraday Materials Laboratory (FaMaL), Materials Research Centre, Indian Institute of Science, Bangalore, 560012, India.*

*b. Materials and Simulation Group, Samsung R&D Institute, Bangalore, 560037, India.*

*c. Materials Science and Engineering Program and Texas Materials Institute, The University of Texas at Austin, Austin, TX 37831, USA.*

*d. Normandie University, ENSICAEN, UNICAEN, CNRS CRISMAT, Caen 14000, France.*

§ authors with equal contribution * prabeer@iisc.ac.in

**Abstract:**

Rechargeable batteries based on Li-ion and post Li-ion chemistry have come a long way since their inception in early 1980s. The last four decades have witnessed steady development and discovery of myriads of cathode materials taking into account their processing, economy, performance along with ecological sustainability. Though oxides rule the battery sector with their high energy and power density, polyanionic insertion compounds work as gold mines for designing insertion compounds with rich structural diversity leading to tuneable redox potential coupled with high structural/ chemical/ thermal stability. The scope of polyanionic compounds can be taken a step further by combining two or different types of polyanions to get suites of mixed polyanionic materials. While most cathodes are built with metal polyhedra constituted by oxygen ($MO_m$ | $XO_m$, M = 3d metals, X = P, S, Si, B, W etc., m = 3-6), in some cases, selected oxygen sites can form bonding with hydrogen to form

$OH/H_2O$ ligands. It can lead to family of hydroxy-based mixed-polyanionic cathode materials. The presence of hydroxy components can affect the crystal structure, local chemical bonding, electronic, magnetic, diffusivity and electrochemical properties. Employing mineralogical survey, the current review renders a sneak peek on various hydroxy-based polyanionic cathode materials for Li-ion and post Li-ion batteries. Their crystal structure, and electrochemical properties have been overviewed to outline future research focus and scope for real-life application.

**Keywords:** batteries; cathodes; polyanions; hydroxy-based insertion materials; capacity.

---

## 1. Introduction

The overdependence of global energy needs on fossil fuels and other non-renewable resources has triggered momentus effort to look for alternate choices. There is a growing demand for clean energy with the ever-increasing population and terawatt-scale energy consumption.[1] Renewable energy resources like solar, wind, geothermal, biothermal etc. are some of the viable alternatives in this regard. Storing energy obtained from renewable energy resources via electrochemical energy storage devices (EES) is an attractive and necessary prospect. Rechargeable metal-ion batteries, based on reversible intercalation of alkali ions into metal-anionic frameworks, are widely used EES for portable electronics. The intercalation principle involving an electronic transfer is a cleaner way of storing electrical energy for various applications. It was first put into practical applications with commercialisation of Li-ion batteries (circa 1991), which led to increased interest and steady development in EES devices for usages ranging from small-scale consumer electronics to large-scale automobiles/ grid storage. At this juncture, the ever-growing consumption of Li-based minerals has raised concerns about the availability of Li resources.[2-4] Moving beyond Li-ion, various other

monovalent/ multivalent alkali chemistry (like $Na^{+}$, $K^{+}$, $Mg^{+2}$, $Ca^{+2}$, $Al^{+3}$ etc.) have also been tested for EES devices based on similar intercalation mechanisms.[5-22] On the basis of the constituent alkali ions, different types of electrochemical behaviour are observed. This is on the account of the different sizes of the alkali metal ions that leads to different properties of materials and stabilizing effects.

Among various intercalation-based cathode materials, two-dimensional (2D) layered oxides have conquered the commercial Li-ion battery sector. Different transition metal oxides like $LiCoO_2$, $NaMO_2$ (M=Transition metal) etc. with stable structure have been explored as robust cathode materials.[11,23-25] Oxides deliver high capacity with good reversibility, although with lower redox potential. To realize high redox potential, three-dimensional (3D) polyanionic materials can be put on anvil to develop structurally diverse cathode systems. Polyanionic materials have strong covalent bonding between the metal-ion redox centre and oxygen atoms, which provide a stable framework and durability for intercalation process. They offer wide range of three-dimensional structures possible with different geometries and linkages. The oxygen atoms present around the metal centres are held tightly in these 3D frameworks. This reduces the chances for release of structural metal/oxygen atoms while charging is done up to higher potentials, thereby increasing the overall safety. Based on inductive effect principle,[26] it is possible to tune the redox potential by choosing polyanionic groups with different electronegativity values. The iono-covalency of the metal-anion bond changes following the inductive effect of the polyanionic groups like phosphates ($PO_4^{-3}$), pyrophosphates ($P_2O_7^{-4}$), fluorophosphates ($PO_4F^{-4}$), sulfates ($SO_4^{-2}$), silicates ($SiO_4^{-4}$), borates ($BO_3^{-3}$) etc.[27-38] Further, mixed polyanionic electrode materials involving different combination of polyanionic subunits [$(XO_4)_m^{-n}$, X = P, S, B, C, S, Si etc.] and/or single anion atoms ($F^{-}$, $Cl^{-}$, $OH^{-}$, $O^{-2}$ etc.) can be explored.[39] Such combinations can lead to variety of cathode materials having exciting new properties with multi electron redox system with superior electrochemical performance.[40-55]

Among these combinations, *triplite* and *tavorite* $LiFeSO_4F$ with combination of sulfate group and fluoride ion exhibit high voltages of 3.9 V and 3.6 V, respectively.[56-59] Introduction of fluoride group increases the overall voltage due to inductive effect along with the stability from the polyanionic group. Although nowadays both fluorine-based electrolytes and binders are available, still the addition of fluorine makes the materials more hazardous and involves safety concerns too. Fluorine is hygroscopic in nature and could possibly form hydrogen fluoride (HF), which is hard to handle in large scale applications. Considering more sustainable alternatives, hydroxide $OH^-$ ion can replace the fluoride group to form hydroxy-based cathode materials. Replacing with $OH^-$ on one hand does slightly lower the redox potential owing to reduced inductive effect, but it can provide higher chemical and thermal stability to materials. Presence of $OH^-$ group leads to additional structural durability along with enhanced resistance to external moisture attack. Keeping these advantages in mind, the current review provides an in-depth overview of various hydroxy ($OH^-$) based battery electrode materials highlighting their uniqueness and versatility for usage in various electrochemical systems including (non)aqueous batteries. Their (low temperature) synthesis, structural features, electronic structure and electrochemical performance have been discussed along with possible future direction to realize hydroxy-based cathode materials. Three major class of electrodes, namely (i) hydroxyphosphates, (ii) hydroxysulfates and (iii) (non) jarosites, have been sketched below.

## 2. Hydroxyphosphates

Hydroxyphosphates based materials, with the general formulae $LiMPO_4.OH$ (M=V, Mn, Fe) combining both phosphate ($PO_4^{3-}$) polyanion and fluoride ($F^-$) ions, form a niche class of battery cathode materials. Due to the structural versatility in polyanionic materials, they can adopt either two-dimensional (2D) or three-dimensional (3D) network structures depending on the constituent alkali and transition metals. The electronegativity of anion can tune the overall

redox potential of transition metal as per the inductive effect. Here, hydroxyphosphate chemistry for Li-ion batteries has been explored (**Table 1**). Although there is no report, these hydroxyphosphates can form a potential family to design post Li-ion (Na/K-ion) batteries.

### 2.1 $LiFePO_4OH$

Simonov et al. and Baur initially investigated the structure of *tavorite* mineral based $LiFePO_4OH$ materials.[60, 61] $LiFePO_4OH$ (LFPOH) was found to crystallize in triclinic structure (s.g. *P*-1), consisting of $FeO_6$ octahedra and $PO_4$ tetrahedra building blocks [**Fig. 1**(a)]. However, due to the small size of Li and H, their exact positions in the structure could not be identified. Marx et al. reported the precise position of Li-and H-atoms with the help of neutron diffraction study coupled with theoretical calculations [Fig. 1(b)].[62] From Fourier difference maps, they claimed the location of Li atoms in the tunnel along *c*-axis, while H-atoms were found linked with oxygen atom shared by two adjacent $FeO_6$ octahedra units. From GGA+*U* method, two sites of lithium were predicted. The first Li site (Li1) that is in close proximity to H-atom was found to be relatively unstable due to electrostatic repulsive forces between them, whereas the second Li site (Li2) was found to be more stable.

Whittingham group first prepared LFPOH by hydrothermal synthesis in 2001, albeit with no electrochemical activity between 1.9 to 4.1 V.[63] Almost a decade later (in 2010), Marx et al. reported its electrochemical activity for the first time. The ball-milled LFPOH delivered a first discharge capacity of 105 mAh $g^{-1}$ at C/50 rate when cycled between 2.0–4.5 V [Fig. 1(c)]. In the first cycle, an irreversible phase transition occurs at 2.35 V (vs. $Li.Li^+$), which is followed by a solid-solution based insertion mechanism in subsequent cycles. Later, Asl et al. reported a unique synthesis employing phosphorous acid as a source of phosphate leading to good quality single crystals.[64] During electrochemical analysis, a discharge plateau was observed at 2.37 V, with an increased additional voltage of 130 mV.[65] It was attributed to the formation of

amorphous $Li_2FePO_4OH$ phase upon first discharge and the upshift in the discharge plateau arose due to subsequent (dis)charge occurring from the amorphous phase. Moreover, due to electrode polarization, huge capacity fading was observed at higher C-rates partly due to its poor electronic and ionic conductivity. Recently, Sharma et al. revisited the electrochemistry of LFPOH by forming micrometric particles with sheet/rod like morphology.[66] In the voltage range of 2.2-4.2 V, LFPOH delivered a stable discharge capacity of 140 mAh $g^{-1}$ ($Q_{Th}$ = 153 mAh $g^{-1}$) at a current density of 1.0 mA $cm^{-2}$ with an average cell potential of 2.6-2.7 V *vs.* $Li^+/Li$ [Fig. 1(d)]. This voltage is slightly higher than the previous reported values, which can be attributed to the particle size reduction by ball-milling. Such increase in cell potential due to particle size reduction has also been reported for $LiFePO_4$ system. The cell showed excellent electrochemical properties with no significant capacity fading up to 60 cycles. Good rate kinetics was observed indicating improved ionic and electronic conductivity in the material due to particle downsizing and carbon coating. Reduced order model (ROM) computation was employed by varying several electrode parameters to gauge the suitability of LFPOH for grid storage.[67] Upon $Li^+/H^+$ ion exchange in LFPOH, a new hydrated form of $FePO_4.nH_2O$ with n=1 was formed.[68] Although both LFPOH and $FePO_4.H_2O$ had similar structure, slight distortion in the polyhedra and the chains changed the symmetry so as to crystallize $FePO_4.H_2O$ in a monoclinic (s.g. *C*2/*c*) structure. The magnetic properties of LFPOH were also studied where a Curie-Weiss type behavior was observed.[69]

### 2.2 $LiMnPO_4OH$

Aranda et al. first studied the structure of $LiMnPO_4OH$ (LMPOH) by neutron diffraction and deuterium substitution of protons. Crystallizing in triclinic framework with *P*-1 space group,[70] lithium atoms were found to be located in the channel along [101] direction. Yang et al. first reported its lithium (de)intercalation in 2012.[71] LMPOH was synthesized by

$H^+/Li^+$ exchange reaction using hydrothermal method. When cycled between 2.0 to 4.6 V at C/100 rate, the lithium half-cell led to an initial discharge capacity of ~110 mAh $g^{-1}$ with an average cell voltage of 3.4 V [Fig. 1(e)]. The first and subsequent (dis)charge curves exhibited different profiles with poor rate capability. At 1C current rate, only 50% of the initial capacity was obtained while no significant retention was observed even at C/100 rate. This poor rate performance can be attributed to the low electronic conductivity of the material, hence warrants suitable carbon coating. However, from *ex-situ* XRD measurements, no amorphization was observed upon (dis)charge. Irreversible phase transformation was observed after the first charge with the retention of overall structure. Kanno group further extended the work on hydroxyphosphates by reporting solid-solution series of $LiMn_{1-x}Fe_xPO_4OH$ over the range $0 \leq x \leq 0.3$ with triclinic structure [Fig. 1(f)].[72] Materials with higher Fe content displayed better electrochemical properties in the voltage range of 2.0 to 4.6 V. $LiMn_{0.7}Fe_{0.3}PO_4OH$ delivered a discharge capacity of 150 mAh $g^{-1}$ with low polarization. This improved performance was attributed to change in the local geometry due to Fe substitution in the structure. The synergic effect in the distortion due to Jahn-Teller effect of $Mn^{3+}$ decreased due to $Fe^{3+}$ substitution. A Curie-Weiss type magnetic behavior was noticed for LMPOH.[73]

### 2.3 $LiVPO_4OH$

Another interesting hydroxyphosphate material is $LiVPO_4OH$ (LVPOH). Unlike Fe and Mn-based materials with limited energy density, LVPOH can deliver high energy density powered by its high redox potential and occurrence of multiple oxidation states of vanadium. Croguennec group reported a detailed study on LVPOH prepared by hydrothermal route.[74] Presence of hydroxyl group and small amount of vanadyl impurity was confirmed by infrared spectroscopy. Nuclear magnetic resonance spectroscopy highlighted the presence of hydroxyl group as the bridging anion between two octahedra [**Fig. 2**(a)]. The lithium diffusion pathways

were studied by means of bond valence sum measurements, revealing one-dimensional $Li^+$ migration along *c*-axis [Fig. 2(b)]. An average cell potential of 3.95 V vs. $Li/Li^+$ was observed when cycled between 3.0-4.6 V [Fig. 2(c)]. A charge capacity of 280 mAh $g^{-1}$ was observed which is double of the theoretical capacity, suggesting the extraction of both Li and H. However, during discharge a large irreversible capacity was observed indicating only one Li insertion into the system. Ex-situ analyses revealed the presence of oxyphosphate $VPO_4O$ phase at the end of charge and $LiVPO_4O$ phase at the end of discharge. A concerted mechanism was suggested as both Li and H are being extracted at same potential. When the material was cycled in the voltage window of 1.2 V to 3.0 V, a discharge capacity of 136 mAh $g^{-1}$ was observed at a potential of 1.4 V vs. $Li/Li^+$ corresponding to one Li-insertion into LVPOH [Fig. 2(d)]. It again proves the advantage of employing vanadium chemistry as multiple electron transfer can occur exploiting multiple oxidation states of vanadium.

### 2.4 Hydroxyphosphates in aqueous batteries

Hydroxyphosphates can also exhibit good electrochemical performance in aqueous electrolytes. Recently, Sharma et al. reported the (de)intercalation properties of LFPOH as an anode in aqueous electrolytes.[66] This was the first report of an Fe-based *tavorite* working as an anode for aqueous LIBs. As these water-based electrolytes are limited by the narrow working voltage window to prevent water splitting on either side, a water-in-bisalt configuration (21 m LiTFSi+7 m LiOTf) was chosen as electrolyte. The use of water-in-bisalt electrolytes enhances the operating voltage window and prevents the formation of SEI during charging. The electrochemistry was performed in a three-electrode setup with Ag/AgCl as reference electrode and Zn sheet as counter electrode. When cycled in the potential window of -1.0 to 1.0 V *vs*. Ag/AgCl, a discharge capacity of 153 mAh $g^{-1}$ was observed at a current density of 1.0 mA $cm^{-2}$ [Fig. 2(e)], retaining ~81% of the initial discharge capacity at the end of 50 cycles. It

exhibited a cell voltage of -0.3 to -0.4 V *vs.* Ag/AgCl, which lies in the anodic range of aqueous batteries. An all-phosphate full cell was assembled using LFPOH as anode and $LiFePO_4$ as cathode. A first discharge capacity of 120 mAh $g^{-1}$ was observed at a cell voltage of 0.8 V with an energy density of 97 Wh $kg^{-1}$ (w.r.t. anode weight) [Fig. 2(f)]. This work showed the possibility to implement hydroxyphosphates in aqueous batteries, which can be extended to other hydroxyphosphate chemistry in aqueous batteries.

### 2.5 Some other hydroxyphosphates

Apart from the traditional hydroxyphosphates discussed above, various materials with different stoichiometry of phosphate and hydroxide polyanion have been reported. They are basically found in various mineral forms across the globe. Although unexplored at this stage, there is a possibility of find electrochemical activity in some of these materials with potential application in rechargeable batteries. Other than the crystal structure, spectroscopic and magnetic properties of these minerals, there is a possibility to study the electrochemical properties of these minerals. A list of such unexplored hydroxyphosphate minerals is provided in **Table 2** along with their chemical formulae.

## 3. Hydroxysulfates

Hydroxysulfates with the general formulae $LiMSO_4.OH$ (M= Mn, Fe, Co) provide another alternative to fluorosulfates and hydroxyphosphates (**Table 3**). The presence of highly electronegative sulfate polyanion instead of phosphate one provides more more ionicity (hence higher redox potential) to constituent transition metal species as per inductive effect. As the sulfate species are water soluble and prone to thermal decomposition, it restricts the possible synthesis routes. In hydroxysulfates, less electronegative $OH^-$ is present instead of $F^-$ species. Consequently, it renders less ionic character of constituent M-X bonds, thereby reducing the

metal redox potential ($M^{n+1/n+}$) by ~0.3 V compared to fluorosulfates. On the other hand, the presence of $OH^-$ species offers enhanced moisture resistance and chemical stability. Reddy et al reported the first hydroxysulfate showcasing monoclinic $FeSO_4.OH$ compound (s.g. *C*2/*c*) as a $Li^+$ (de)intercalation host.[75] The target compound was prepared by annealing commercial $FeSO_4.7H_2O$ precursor at 280 $^0$C for a week. Its crystal structure is composed of $FeO_4(OH)_2$ octahedra (corner shared), with four equatorial oxygen bridged together by four sulfate ($SO_4^{-2}$) tetrahedra [**Fig. 3**(a)]. These corner-shared octahedra form parallel chains along the *a*-axis with spaces for $Li^+$ insertion. It led to a reversible capacity ~150 mAh.g$^{-1}$ involving an $Fe^{3+}/Fe^{2+}$ redox activity centered at 3.2 V [Fig. 3(b)]. The electrochemical $Li^+$ insertion involved a biphasic mechanism with the formation of *tavorite* $Li_xFeSO_4OH$ (x approaching 1) endproduct with triclinic (*P*-1) structure.

Inspired by the structural similarities present between $FeSO_4OH$ and $FeSO_4F$, Ati et al. prepared the solid-solution family of $FeSO_4F_{1-y}OH_y$ ($0 < y < 1$) using $Fe_2(SO_4)_3.nH_2O$ and $FeF_3$ precursors.[76] The reaction was carried out at 300 $^0$C for 50 h and the structural water content was adjusted by varying the annealing time from 30 minutes to several hours. Overall, monoclinic frameworks (s.g. *C*2/*c*) were obtained consisting of $FeO_4(F,OH)_2$ octahedra abridged together via either OH or F species. These chains were in turn connected by $SO_4^{2-}$ polyanionic groups to form a 3D framework [**Fig. 4**(a,b)]. This one step synthesis led to the $FeSO_4F_{1-y}OH_y$ phases with electrochemical performance ranging from 3.6 V to 3.2 V with decrease in the F/OH ratio. The lithium (de)insertion mechanism was also shown to be dependent on the F/OH ratio [Fig. 4(c)]. *In-situ* XRD and Mössbauer measurements revealed the formation of an intermediate $Li_{0.5}Fe_{0.5}^{+3}Fe_{0.5}^{+2}SO_4OH$ during the (dis)charging step. Possibility of using similar method for synthesizing metal-substituted $Fe_{1-x}M_xSO_4F_{1-y}OH_y$ (M = Ti, V) was also demonstrated.

Following, mesoporous $LiFeSO_4F_{0.44}(OH)_{0.56}$ was reported prepared by a two-step route.[77] This synthesis involved manual mixing of the precursors with the resultant paste kept at 45 ºC for 60 h. Finally, heating was done at 120 ºC to get the end product. Mesoporous morphology helped in longer durability and superior cyclability than previously reported fluorosulfate like cathodes. During galvanostatic cycling, a clear intermediate phase $Li_{0.5}Fe_{0.5}^{+3}Fe_{0.5}^{+2}SO_4F_{0.56}(OH)_{0.44}$ was observed as reported by Ati et al (mentioned above), corresponding to the triclinic $LiFeSO_4F_{0.56}(OH)_{0.44}$ to monoclinic $FeSO_4F_{0.56}(OH)_{0.44}$ transition. 80 % capacity retention was observed upto 2800 cycles without any carbon coating or particle downsizing. Power density was found to be 5.9 kW $kg^{-1}$ at 15C and 20.4 kW $kg^{-1}$ at 30C. These values reported are one magnitude higher than commonly reported values for Li-ion batteries. Optimization of various synthesis processes can lead to improved electrochemical properties for the hydroxy-fluorosulfates $LiFeSO_4F_y(OH)_{1-y}$.

As it is difficult to prepare the 3.2 V $LiFeSO_4OH$ cathode via solution-based methods, Subban et al. employed mechanical-milling route, which led to the discovery of a new monoclinic polymorph. LiOH and $FeSO_4$ (anhydrous) were ball milled to get a mixture containing $Li_2SO_4$ and a *caminite* mineral type intermediate phase $Fe_3(SO_4)_2(OH)_2$.[78] Though this phase was electrochemically inactive, it formed $LiFeSO_4OH$ in the presence of excess LiOH and $Li_2SO_4$. Other isostructural analogues were also prepared by using $MSO_4$ (M = Co, Mn) and $Li_2SO_4$ mixture and annealing at varying temperature range of 185-250 ºC. Interestingly, only the Fe analogue could be directly prepared form the *caminite* type mineral simply by mechanochemistry (ball milling), while other analogues (Co, Mn, Ni) required further annealing to yield the final products. Overall, the layered isostructural $LiMSO_4OH$ (M=Mn, Fe, Co) analogues [**Fig. 5**(a)] can be formed either using a mechanochemical route or a ceramic one. The layered $LiFeSO_4OH$ phase obtained from the above-mentioned procedure had a monoclinic structure having a $P2_1/c$ symmetry [Fig. 3(d)]. It consists of layers of

$FeO_4(OH)_2$ octahedra joined together in an edge sharing fashion. Zigzag chains are formed in [010] direction joined with the help of the $FeO_6$ octahedra vertices to form a layered structure with sulfate units present above and below it. $Li^+$ ions are present in the cavities formed between adjacent layers.

Layered $LiFeSO_4OH$ hydroxysulfate exhibits an operating voltage of 3.6 V for Li ion intercalation unlike its monoclinic analogue having 3.2 V activity [Fig. 3(e)]. This potential difference between two polymorphs is explained via the configuration of the polyhedra present in the crystal system. In case of layered $LiFeSO_4OH$, $FeO_6$ octahedra building blocks are edge shared that leads to repulsion between the neighbouring $Fe^{+3}$ ions in the charged state enhancing the overall Gibbs free energy of the system [Fig. 3(d)]. While the high-voltage monoclinic (layered) $LiFeSO_4OH$ underwent a solid solution (single-phase) behaviour, the lower-voltage polymorph exhibited a biphasic redox behaviour with flat voltage profile. Similar structure-property relationship has earlier been noticed in case of $LiFeSO_4F$ fluorosulfate polymorphs.

Theoretical studies involving DFT calculations and atomistic modeling on the layered (monoclinic) and *tavorite* (triclinic) $LiFeSO_4OH$ polymorphs show sinusoidal 2D Li-ion migration pathways. The layered polymorph shows a lesser activation energy barrier of ≈0.2 eV than the *tavorite* one (≈0.7 eV), making it more suitable choice for cathode material.[79] The ion migration pathways for both polymorphs are illustrated in Fig. 3(c,f). Long range diffusion is possible in the case of layered polymorph owing to its lower activation barrier. Notably, while doing the theoretical studies, van der Waals interaction play a major role in finding accurate values for the data, i.e. crystal structure, cell voltage, interlayer spacing etc. Also, the hydrogen atom present was found to be immobile albeit with stationary vibrations. Defect properties of these hydroxysulfate cathodes were analyzed by computational tools. Exchange of $Li^+$ ion with $Fe^{+2}$ ion (i.e. anti-site defects) was noticed in both $LiFeSO_4OH$ polymorphs. However, the degree of anti-site defects was very low (lesser than $LiFePO_4$).

Among all 3d-metal based hydroxysulfates, the Fe-analogue ($LiFeSO_4OH$) was found to show efficient reversible $Li^+$ (de)intercalation with the insertion of 0.8 $Li^+$ ions per formula unit (pfu). On the other hand, $LiCoSO_4OH$ showed high-voltage redox activity at 4.8 V albeit with poor $Li^+$ insertion (i.e. 0.2 $Li^+$ ions pfu). $LiMnSO_4OH$ was found to be completely inactive [Fig. 5(d)].[78] For layered $LiFeSO_4OH$, *in-situ* XRD studies revealed a gradual and reversible shifts in peak positions implying a solid-solution (monophasic) redox mechanism [Fig. 5(b)]. Although a split peak was observed in the derivative curve for $LiFeSO_4OH$, no corresponding structure feature was confirmed by *in-situ* studies. During cathode cycling, a volume change of ~7% was observed (similar to $LiFePO_4$), while the *tavorite* $LiFeSO_4OH$ underwent ~10% volume change.

Badrudin et al studied the effect of lithium (de)intercalation in layered $(Li)FeSO_4OH$ using first principle calculations using stable antiferromagnetic configuration.[80] Present $Li^+$ ions were found to be strongly ionic in nature, thereby limiting probability of complete delithiation of the material. Change in the Fe 3d orbital contribution in conduction and valence bands was observed according to the movement of Li. That in turn led to the conclusion that changing the transition element could pave a way for improving the battery performance. Subsequently, Badrudin et al utilised this concept to yield better electrochemical performance with vanadium (V) substitution in $LiFeSO_4OH$.[81] $LiFe_{0.75}V_{0.25}SO_4OH$ was formed theoretically signifying a decrease in the overall band gap of the material with increase in the electronic conductivity. V substituion led to (~4%) expansion of unit cell volume that in turn ease the migration of lithium ions. Overall, vanadium substitution leads to increase in ionic as well as electronic conductivity. Enhanced battery stability can be obtained by the vanadium substitution while (dis)charging the battery.

Radha et al investigated the thermodynamic stability of the $LiMSO_4OH$ (M=Mn, Fe, Co) hydroxysulfate family using isothermal acid calorimetry.[82] A decrease in thermal stability was observed with increase in the ionic radius (i.e. from Co- to Mn-analogue) [Fig. 5(c)]. The *tavorite* $LiFeSO_4OH$ polymorph was found to be less stable than the layered one. It is due to the presence of corner sharing octahedra in *tavorite* case and edge sharing octahedra in the layered one. Distortions along with the sulfate group control the thermodynamic and electrochemical behaviour. As the symmetry changes from $C_{3v}$ to $C_{2v}$, decrease in the electrochemical performance and redox potential was observed. Redox potential decreases with decrease in exothermic enthalpy of formation [Fig. 5(e)]. As we go from Mn to Co, the exothermic enthalpy increases and thus redox potential also increases. This can be correlated to the smaller size of Co than other analogues and thus stronger bonds. This study also provides an answer for the inactivity of Mn analogue ($C_{2v}$), as its enthalpy of formation is really low.

Using DFT analysis of electronic structure along with optical properties of the layered $LiMSO_4OH$ family,[83] $LiFeSO_4OH$ was found to be a direct band gap semiconductor. After the analysis of the (non)polar covalent bonds and frequency dependent optical properties, $LiFeSO_4OH$ was found to have photoelectric properties with potential application in optoelectronic devices. In addition, thermoelectric property was noticed in heavily doped $LiFeSO_4OH$ at varying temperatures (300 to 750 K) with a large Seebeck coefficient value of around 400 μV/K.

The presence of OH- species render moisture resistance to hydroxysulfate vis-à-vis fluorosulfate. Zhang et al studied the effect of relative humidity on the structure and electrochemical properties of $LiFeSO_4F$ material.[84] Surprisingly, there was a partial degree of *in-situ* formation of $LiFeSO_4OH$, when $LiFeSO_4F$ was cycled in the electrochemical cell due to the presence of humidity. Degradation of the *tavorite*-type $LiFeSO_4F$ to $FeSO_4.nH_2O$ and

LiF was observed with relative humidity of 62%, which then partially converts to $LiFeSO_4OH$ within the cell as evident from deviation in voltage profiles. This *in-situ* formation of $LiFeSO_4OH$ offers another approach to form metastable phases worth further exploration.

## 4. Jarosites

Moving on from lithium-based hydroxysulfates, we examined jarosite family of compounds having sodium and potassium based hydroxysulfate members. Jarosites belongs to the *alunite* super group of minerals, where original *alunite* is a hydroxylated aluminium based minerals with formula $KAl_3(SO_4)_2(OH)_6$. While *alunites* can be composed of various moieties ($PO_4$, $AsO_4$ etc), jarosite sub-group of minerals solely contain $SO_4$-based moieties (**Table 4**). These compounds have similar polyanions (i.e. $SO_4^{2-}$ and $OH^-$), but in different stoichiometry, thereby offering diversity in structural and electrochemical properties. Jarosite mineral, generally a hydrous sulfate of potassium and ferric ($Fe^{3+}$) iron [$KFe_3(SO_4)_2(OH)_6$], was discovered in 1852 by August Breithaupt. The mineral is named after the place of discovery, Barraco del Jaroso, Almeria, Spain.[85] The name is fitting as the mineral crystal has yellowish color (Jara, Spanish name of a yellow flower). As evidence of water on Mars,[86] Jarosite has been detected by three martian rovers: Curiosity, Spirit and Opportunity.[87-90] While jarosite is naturally formed by oxidation of pyrite ($FeS_2$) in presence of water, it can be obtained as an industrial byproduct during the purification and refining of zinc.

### 4.1 Crystal structure of Jarosite

Jarosite crystals stabilize in trigonal system with space group $R\bar{3}m$ (#166-1). The structure is composed of 2D corrugated layers formed by linkage of transition metal octahedra [$FeO_2(OH)_4$] and sulfate tetrahedra ($SO_4$), which is stacked along *c* direction. Each transition metal occupies crystallographically equivalent site (2/m) and forms octahedra having 4 [$OH^-$] units attached in the equatorial plane and 2 O along the axial positions. Any two octahedra are connected along the equatorial corners, while metal octahedra and sulfate tetrahedra are

connected along the axial oxygen. Each sulfate tetrahedra shares 3 corners with metal octahedra forming a unique trimer unit, while the fourth unshared oxygen corner points alternatively below and above 2D layer. These are present along the direction of hexagonal ring formed by three trimer-units [**Fig. 6**(a)]. The alkali ion resides in the open spaces at '3a' in the layer containing sulfate tetrahedra. This arrangement leaves open space for guest alkali ion at '3d' and '9e' sites.[91] The presence of open space hexagonal ring in the corrugated layers is like that of hexagonal tungsten bronze (HTB) slabs and Kagomé-like structure [Fig. 6(b)]. The resilient crystal structure of Jarosite allows a range of substitution of (i) $Fe^{3+}$ ions by other metal ions in +3 oxidation states such as $V^{3+}$, $Cr^{3+}$, $Al^{3+}$, $Ga^{3+}$, $In^{3+}$ etc., (ii) $K^+$ ions by $NH_4^+$, $Na^+$, $K^+$, $H_3O^+$, $Ag^+$, $Tl^+$, $½Pb^{2+}$, $½Hg^{2+}$ etc., and (iii) $SO_4^{2-}$ polyanions by $SeO_4^{2-}$, $CrO_4^{2-}$ etc.[92,93] The nature of transition metal, capping polyanionic unit and alkali ion in the interlayer region affect the bond distance among intralayer trimer units and interlayer spacing. Further, the stoichiometry of Jarosite compounds is highly dependent on the synthesis route, such as conventional rapid precipitation route[94] and kinetically slow redox-based hydrothermal method.[95]

### 4.2 Magnetism in Jarosite compounds

Jarosites have long been studied for their magnetic property arising from magnetic frustration engendered by geometry of the lattice. Jarosites, a member of *Kagomé* lattice family, has the corner connected trimer units of $[FeO_2(OH)_4]$ octahedra capped by sulfate tetrahedra resulting in spin frustration at the $Fe^{3+}$ ($d^5$, S=5/2) metal centres coupled by nearest neighbour Fe-O-Fe super-exchange interaction (antiferromagnetic interaction).[96-99] As jarosites offer structural flexibility by accommodating ion substitutions at $K^+$, $Fe^{3+}$ and $SO_4^{2-}$ sites, this family of compounds has become model systems for examining spin frustration and resultant bulk magnetic behaviour as a function of (i) interlayer spacing, (ii) interlayer alkali ions (iii) intra-layer metal ions, (iv) capping polyanion, and (v) M-O-M bond distance. The spin arrangement in the triangular *Kagomé* lattice of Jarosite results in infinite number of degenerate

ground states [Fig. 6(c)], therefore, ideally it should not exhibit long-range magnetic ordering (LRO) at temperature T > 0 K. However, jarosite compounds do exhibit LRO as $AFe_3(SO_4)_2(OH)_6$: A= $NH_4^+$, $Na^+$ and $K^+$ undergo antiferromagnetic ordering at ~55 K, 53 K and 60 K respectively with each 2D-layer itself acting as compensated antiferromagnet.[100] Possibly, spin frustration induced ground-state degeneracy is abolished by perturbations such as next-to-nearest neighbour exchange interactions, spin anisotropy and lattice disorder. In case of Fe-jarosite, the LRO was ascribed to weak single-ion anisotropy developed due to Dzyaloshinsky-Moriya interaction.[101] Later, experimental evidence of lattice disorder affecting LRO was confirmed as magnetic ordering temperature decreased for stoichiometrically pure V-jarosites prepared by novel redox-based hydrothermal route compared to non-stoichiometric compounds obtained using conventional precipitation route.[95] Interestingly, the extent of antiferromagnetic exchange interaction decreases with transition metal centers having lower number of electrons in d-orbital.[102] Finally, the $V^{3+}$ ($d^2$) jarosite shows ferromagnetic exchange within the Kagomé layer with interlayer antiferromagnetic coupling dependent on the interlayer spacing.[103] Monocation substitution has been used as a tool to change interlayer space of Jarosites and observe its effect on LRO temperature. Such investigation on Fe and Cr-jarosites did not reveal any trend in Néel-temperature, while a monotonic increase in Curie temperature with decreasing interlayer spacing was observed for monocation substituted V-jarosites. This is attributed to nature of super-exchange M-O-M interaction in Fe and Cr-jarosite, which is directly dependent on M-O bond covalency that remains unaffected to cationic substitution. However, the bonding nature in transition metal polyhedra of $KFe_3(SO_4)_2(OH)_6$, especially the Fe-$O_{eq}$ (equatorial oxygen), apart from interlayer space and interlayer H-bonding has been shown to change under external pressure.[104] With increase in applied pressure on single crystal of K-Fe-jarosite, first the interlayer spaces are reduced followed by increase in interlayer H-bonding and finally the shortening of Fe-$O_{eq}$ occurs resulting in an increase of metal-ligand

covalency. The increased metal-ligand covalency and hence increased orbital overlapping induces stronger intra-layer antiferromagnetic ordering. Thus, K-Fe-jarosite exhibits a monotonic but non-linear increase in Néel temperature under applied pressure.

### 4.3 Jarosite as electrode for metal-ion batteries

Over the last decade, various jarosites and their derivatives have been examined as potential cathodes for metal-ion batteries. Some principal examples are summarised in **Table 5**. The first example of Jarosite family member as insertion cathode for Li-ion battery was reported by Gnanavel et al (circa 2014) focusing on Natrojarosite $NaFe_3(SO_4)_2(OH)_6$.[105] Solution drying route was used to quickly saturate and precipitate the titular product at 90 °C for 48 h (in air), followed by washing with distilled water and overnight drying at 110 °C. Initially, the solution was prepared by dissolving $Na_2SO_4$ and $Fe_2(SO_4)_3.nH_2O$ in molar ratio of 1:2 in 0.01 M $H_2SO_4$. Considering a reversible (de)insertion of 3 Li per f.u. of $NaFe_3(SO_4)_2(OH)_6$, a theoretical capacity of 166 mAh/g was calculated. During galvanostatic cycling at C/20 rate, natrojarosite allows insertion of 2.1 $Li^+$ per f.u. during first discharge and deinsertion of 2 $Li^+$ during subsequent charging step, thus delivering a reversible capacity of 110 mAh/g at 2.82 V (vs. $Li/Li^+$) [**Fig. 7**(a,b)]. Noteworthy is the flat shape of first discharge curve reminiscent of biphasic reaction mechanism, which is distinctly different from subsequent (dis)charge cycles having slopping profile due to topotactic reaction mechanism.[105] By synergizing *ex situ* XRD and TEM analysis, it was shown that the host cycles reversibly between crystalline to amorphous state [Fig. 7(c,d,e)]. The biphasic reaction during first discharge is perhaps due to the formation of defects beyond a critical lithium concentration in the structure in the form of $FeO_5$ pyramids from original $FeO_6$ octahedra, thereby, inducing strains in the 2D layers $[Fe_3(SO_4)_2(OH)_6]$ of the host structure. It leads to the formation of inorganic polymer from pristine host whose strains reversibly relaxe on $Li^+$ deinsertion forming original crystallized structure [Fig. 7(f)]. The $Na^+$ (de)insertion in Natrojarosite is also

governed by the same reaction mechanism with reversible capacity of 120 mAh/g at a rate of C/20 with $Fe^{3+}/Fe^{2+}$ redox couple centered ~2.72 V (vs. $Na/Na^{+}$).[106]

Plugging the gap of a rigorous mechanistic study of $Li^{+}$ intercalation in Natrojarosite $NaFe_3(SO_4)_2(OH)_6$, Kosova et al. published their analysis based on synergized theoretical and experimental studies.[107] Natrojarosite was synthesized using hydrothermal synthesis route by dissolving $Fe_2(SO_4)_3.9H_2O$ and $NaHSO_4.H_2O$ reagents in 0.01 M $H_2SO_4$ under agitation. The hydrothermal reaction was completed in a teflon autoclave at 150 °C for 48 h. Following, the precipitate was washed and dried in vacuum oven at 90 °C for 8h before intimately mixing with conductive carbon to obtain the electrode composite. It exhibited bi-phasic crystalline-amorphous transformation during first discharge on Li and Na insertion, in sync with earlier results. The structural rearrangement would occur to facilitate alkali ion migration which otherwise would not be allowed in the narrower ion conducting channels of natrojarosite. Change in intercalation mechanism from biphasic to solid solution during first cycle had a dramatic effect (two orders of magnitude) on the alkali ion diffusion coefficients of Li/Na ion [**Fig. 8**(a)]. After 10 cycles at C/20 current rate, a reversible capacity of 71 mAh/g was observed against Li metal anode with two redox peaks at (i) 2.71/2.63 V and (ii) 3.03/2.93 V attributed to Na and Li (de)intercalation phenomenon like that of sodium-iron carbonophosphate. The intensity of first redox peak diminished with further cycling indicating formation of a thermodynamically stable mixed phase $Na_{1-x}Li_xFe_3(SO_4)_2(OH)_6$, predicted based on DFT calculation, from which subsequent Li (de)intercalation can occur [Fig. 8(b,c)]. After same cycle and current rate for $Na^{+}$ intercalation, the stable reversible capacity stood at 80 mAh/g for ~ 1.4 alkali ion uptake with average redox potential of 2.55 V. Based on suites of ex situ analyses, several conclusion were drawn. First, partial reversibility of crystalline-to-amorphous transformation after first discharge was observed. The structure breaks down completely after $30^{th}$ cycle evidently with appearance of $Li_2SO_4.H_2O$ and $Fe_2O_3$ [Fig. 8(d)]. Second, in contrast

to earlier assumption of generation of $FeO_5$ pyramidal defects units during discharge, a constant presence of $Fe^{3+}$ in octahedral environment was observed during cathode cycling [Fig. 8(e)]. Thus, $Li^+$ insertion during first discharge strongly distort $SO_4$ and $FeO_6$ polyhedra resulting into disordering of the bulk structure and amorphization. Finally, the crystalline-amorphous transformation of natrojarosite host was found to be irreversible after 30$^{th}$ cycle with appearance of $Li_2SO_4.H_2O$ and $Fe_2O_3$ phase.

The discovery of natrojarosite as promising cathode host for Li- and Na-ion batteries prompted further investigation of analogous compounds of jarosite family. In this pursuit, the original potassium-jarosite $KFe_3(SO_4)_2(OH)_6$ was fabricated in 2D nanostructure form at room-temperature via facile, scalable and economic template-assisted redox precipitation route [**Fig. 9**(a,b)].[108] Nanosheets of δ-$MnO_2$ was used as both oxidant and self-sacrificing template. Stoichiometric amounts of $FeSO_4.7H_2O$ and $KNO_3$ were added into a brown colloidal suspension of δ-$MnO_2$ nanosheets kept under magnetic stirring. The change in color of suspension from brown to orange in ~ 10 minutes signaled reaction completion. Following, the suspension was aged for 12 h at room temperature before washing with deionized water and ethanol, and vacuum drying. It led to 2D nanostructured morphology with 5-10 nm buiding blocks having thickness of ~13 nm and surface area of 71 $m^2g^{-1}$. 2D nanosheets of natrojarosite could also be fabricated using the same template-assisted route. Like the $Li^+$ (de)intercalation in natrojarosite, jarosite also exhibited a biphasic reaction with plateau around 2.3 V in the first discharge curve. Subsequent charge-discharge step showing sloppy profile at average potential of 2.87 V and 2.09 V, respectively, which can be attributed to topotactic reaction mechanism. Barring the first discharge step, a capacity of 111 mAh/g was reversibly attained indicating a (de)intercalation of 2.1 Li per formula units at a current rate of C/10. Even at 10 C rate, a reversible capacity of 75 mAh/g was recorded. Essentially, the enhanced Li storage performance of jarosite was attributed to its special 2D nanostructured morphology facilitating

fast $Li^+$ diffusion and electron transport, higher surface area offering more reaction points for $Li^+$ (de)insertion and good structural integrity under lattice strain during galvanostatic cycling.

When the 2D nanostructured jarosite was galvanostatically cycled in the voltage range of 0.005- 3.0 V vs. $Li^+/Li$, it showed promises to work as a conversion reaction-based anode material exhibiting high capacity, rate capability and cycling life [Fig. 9(c)].[109] At a current density of 100 $mAg^{-1}$, the as prepared jarosite exhibited first discharge and charge capacities as 1786.7 and 1300.8 mAh $g^{-1}$, respectively, which is more than thrice the theoretical capacity of 481 mAh/g estimated solely on complete reduction of $Fe^{3+}$ to $Fe^0$ involving 9 $Li^+/9e^-$ reaction. This implied that the extra capacity stems from intermediate reactions. Synergistic analysis of ex-situ XRD and XPS measurements revealed the conversion reaction mechanism as follows. During first discharge to 1.5 V, Li insertion into $KFe_3(SO_4)_2(OH)_6$ takes place resulting into formation of $Li_xKFe_3(SO_4)_2(OH)_6$ ($x \leq 3.7$), which gradually disappears on continuous discharge to 1.0, 0.6 and 0.005 V giving way to the appearance of LiOH. Further, $Li_2S$ formation is detected in XPS which would stem from $Li_2SO_4$ involving $8e^-$ transfer for an additional theoretical capacity of 1948 mAh/g. On subsequent charge, new phases evolve: FeOOH, $\gamma$-$Fe_2O_3$, $Li_2SO_4$ and $LiKSO_4$ [Fig. 9(d)]. Overall, the jarosite undergoes an irreversible conversion reaction during first cycle. Despite the complexity of phase evolution during conversion reaction, the reversibility is retained even after 600 cycles with capacity of 1350 mAh/g at 1 A/g [Fig. 9(e)]. In addition, the 2D nano-architecture was structurally stable after 100 cycles at 500 mA/g, owing to formation of a protective shell around nanobuilding blocks which can accommodate the volume change during conversion reaction cycle, apart from shielding the core from electrolyte corrosion [Fig. 9(f)]. Similar results were reported for 2D nanostructured natrojarosite.

Following another facile and scalable solution-phase oxidation process, a 2D jarosite@rGO composite was reported as suitable insertion host for Li-ion batteries.[110] The

synthesis route was similar to the template-assisted route discussed earlier, however the single-layer graphene oxide (GO) nanosheet as template was non-sacrificial, which was reduced in hydrazine hydrate solution at 25 °C to get rGO. Here, the rGO provides an edge in terms of high electrical conductivity, mechanical strength, and flexibility to Jarosite, which can enhance the capacity, rate capability and cycling stability. The jarosite@rGO composite delivered a first discharge and charge capacity of 143.7 and 146.8 mAh/g (~2.5 Li uptake per f.u.) respectively (vs. $Li/Li^+$). Even after 300 cycles at 10 C rate, the composite showed a capacity of 70.7 mAh/g.

Replacing the $Fe^{3+}$ transition metal center in $AFe_3(SO_4)_2(OH)_6$ [A= $Na^+$, $K^+$, $NH_4^+$, $H_3O^+$] with $V^{3+}$ leads to another member of Jarosite family, known as vanadium (V) jarosite. Jarosite and V-jarosite (where A = Na, K and M = V, Fe) were synthesized in microwave hydrothermal reactor using iron (III) chloride and vanadium (III) chloride as the source of Fe and V metal, respectively.[111] Alkali (Na/K) sulfates were employed as alkali and sulfate source with concentrated sulphuric acid serving as pH controller crucial to product precipitation. The micrometric morphology of as-synthesized products exhibited dependance on composition. Natrojarosite powders were faceted in contrast to the jarosite having micrometric aggregates of rounded particles. On the other hand, V-natrojarosite powders showed rose-like aggregates morphology, while V-jarosite powders were rounded and pill-shaped with smooth surfaces. Additionally, compositional deviation from stoichiometric $AM_3(SO_4)_2(OH)_6$ formula was observed. The deviation can occur in two ways: (i) substitution of hydronium ion ($H_3O^+$) at A site in the interlayer region resulting in deficiencies of $A^+$, and (ii) $M^{3+}$ deficiencies triggering formation of $H_2O$ following protonation of interlayer hydroxyl group, under charge neutrality condition.[95] The $Li^+$ insertion chemistry of these samples were similar to that discussed above, albeit with poor cycling stability attributed to lower fraction of conducting carbon black in the electrode composite and larger particles size of pristine materials. With further optimization, V-natrojarosite and V-jarosites can be promising electrode candidates for Li-ion batteries.

Moving away from monovalent alkali ion-based jarosite, recently an isostructural divalent Pb-based jarosite having formula $Pb_{0.5}Fe_3(SO_4)_2(OH)_6$ was reported as cathode material for Li-ion batteries.[112] There are two main advantages of Pb substitution in jarosite system. The aliovalent substitution of divalent $Pb^{2+}$ for monovalent $Na^+$ in parent jarosite structure can create vacancies and expedite facile alkali-ion migration during (de)insertion reaction. Further, the higher electronegativity of Pb (1.9) vis-à-vis Na (0.9) can induce secondary inductive effect in the system by drawing electron density away from coordinated oxygen ions, thereby decreasing the Fe-O covalency and eventually increasing the $Fe^{3+}/Fe^{2+}$ redox potential.

The prepared Pb-jarosite was found to have $[Pb_{0.33}(H_2O)_{0.33}{}^{0.33}]Fe_3(SO_4)_2(OH)_6$, composition corroborating the expected vacancy at A site. Cyclic voltammograms (at 0.1 mV/s) of Pb-jarosite revealed two reduction peaks at 2.3 V and 2.5 V, and one oxidation peak at 2.6 V (vs Li metal anode). Notably, at current rate of C/5, the Pb-jarosite exhibited first discharge capacity as 91.4 mAh/g (1.93 $Li^+$) which is higher than corresponding value for Na-jarosite (89.8 mAh/g, 1.62 $Li^+$). Compared to Na-jarosite, the average $Li^+$ diffusion coefficient was estimated to be 10 times larger for Pb-jarosite which was attributed to A site vacancy. Over prolonged cycling, the Pb-substituted jarosite showed more structural resilience to irreversible amorphous transformation than Na-jarosite, which becomes increasingly amorphous over 50 cycle. It can be ascribed to larger $Pb^{2+}$ cation pinning the layered crystal structure together. Overall, Pb-jarosite opens avenues for further investigation of jarosites as economic cathode material for weight independent battery applications.

**4.4 Non-jarosite hydroxy-sulfates**

Exploring jarosite chemistry and its derivatives, recently $K_2Fe_3(SO_4)_3(OH)_2(H_2O)_2$ was reported as a new hydroxysulfate cathode material with high-rate capability for all three alkali ions ($Li^+$, $Na^+$ and $K^+$).[113] This non-jarosite layered hydroxysulfate compound is isomorphous to $K_2Co_3(SO_4)_3(OH)_2(H_2O)_2$ assuming an orthorhombic crystal system with $Cmc2_1$ symmetry.

The compound was synthesized using hydrothermal route at 160 °C for 48 h, leading to hexagonal powder morphology (0.3-1 μm) with exposed facets assigned to (100), (011) and (001) crystal planes. The cathode composite exhibited equally good insertion electrochemistry for Li, Na and K alkali ions. When tested in half-cell configuration against Li/Na/K metal anode, structural $K^+$ ion was removed at 3.0 V and corresponding alkali ions were reinserted below 3.0 V through a solid-solution mechanism. In case of Li half-cell, two reversible redox couples were observed at 2.5/2.2 V and 3.2/3.0 V attributed to $Fe^{2+}/Fe^{3+}$ redox activity. For Na and K half-cells, the $Fe^{2+}/Fe^{3+}$ redox couple was centered around 3.1/2.6 V and 3.3/2.8 V, respectively. $Li^+$ ions were predicted to migrate in a 2D path in the inter-layer region, whereas $Na^+$ and $K^+$ ions were structurally restricted to 1D migration. At 0.2 C rate, this cathode material exhibited a capacity of 120 mAh/g, 110 mAh/g and 100 mAh/g for $Li^+$, $Na^+$ and $K^+$ insertion, respectively with excellent cycling stability. Even at high rate (10 C), $K_2Fe_3(SO_4)_3(OH)_2(H_2O)_2$ material delivered capacities of 65 mAh/g, 55 mAh/g and 45 mAh/g respectively, thereby offering its candidacy as a high-rate performance cathode material. Non-jarosite derivatives warrants further exploration to unveil new batery insertion materials.

## 5. Perspectives and Summary

From synthesis perspectives, the hydroxyphosphates ($A_xMPO_4OH$) can be scalably prepared either via conventional solid-state or hydrothermal routes. While, the $SO_4$-based candidates (hydroxysulfates and jarosites) can be produced involving energy-savvy low temperature (T < 400º C) routes. Caution must be exercised during heat treatment as the $SO_4$-based compounds are prone to thermal decomposition evolving $SO_x$ gases. Nevertheless, all hydroxy-based cathode materials offer an advantage in terms of moisture resistance. While many oxides and polyanionic compounds (particularly electrodes with redox potential ≤ 3 V like $LiFeBO_3$ and fluorinated cathodes like $FeF_3$, $LiMSO_4F$, $LiMPO_4F$) suffer from moisture attack, the presence of $OH^-$ species in hydroxy-based cathodes make them moisture-resistant.

The electrochemical performance of various hydroxy-based cathodes, namely (i) hydroxyphosphates, (ii) hydroxysulfates and (iii) (non)jarosites, have been summarised in **Fig. 10**. While majority of them work as voltage below 3 V, layered $LiFeSO_4OH$ (3.6 V) and *tavorite* $LiVPO_4OH$ (~4 V) offer high-voltage activity and thus high energy density comparable to commercialized $LiFePO_4$. It is key to note several of these hydroxy-compositions are capable of multiple-electron redox activity leading to high capacity. These cathodes can be further optimized using techniques like particle nanoscaling, homogenization, and coating by conductive carbon layers and/or ionic conducting ceramics (like $Al_2O_3/ZrO_2$).

While these compounds are widely tested for metal-ion batteries, selected compositions (with emphasis on Co and Ni) can be exploited for electrocatalytic activity. As the hydroxy-based compositions can be stable in water, they can work as electrocatalytic materials with oxygen evolution and oxygen reduction (OER and ORR) reactions. Selected compounds may demonstrate potential for usage in metal-air batteries.

Polyanionic class of materials have long been the treasurehouse to unveil structurally diverse electrode materials with tuneable redox potential. On another note, earth's crust is rich with myriads of hydroxy-based (hydrated) mineral compositions. Exploiting crystallographic and mineralogical databases, hydroxy-based compositions and their synthetic derivatives can be tested to unravel new battery insertion materials. The current review attempts to summarize existing cathode materials exclusively containing hydroxy ($OH^-$) moieties. The presence of $OH^-$ triggers variation in crystal structure, materials stability and magnetic properties. Among them, three best compounds were found to be (i) *tavorite* $LiVPO_4OH$ (4 V), (ii) $LiFeSO_4OH$ (3.6 V) and (iii) jarosite $KFe_3(SO_4)_2(OH)_6$ (2.58 V). These hydroxy-based insertion materials offer a fertile ground for materials discovery, crystallography, and fundamental research on electronic, magnetic and electrochemical properties.

**Acknowledgements**

We acknowledge the financial support from the Technology Mission Division (Department of Science and Technology, Government of India) under the aegis of Materials for Energy Storage (MES-2018) program (DST/TMD/MES/2K18/00217). SL thanks Dr. S. Adiga for hosting him at Samsung Research Institute for research internship. LS is grateful to the Electrochemical Society (ECS, USA) for the 2020 ECS F.M. Becket Summer Fellowship. The crystal structures were illustrated with the help of VESTA software.[120]

**References:**

1. R. E. Smalley, *MRS Bull.*, 2005, **30**, 412-417.
2. J.-M. Tarascon, *Nat. Chem.*, 2010, **2**, 510.
3. A. Sonoc and J. Jeswiet, *Proc. CIRP.*, 2014, **15**, 289-293.
4. E. A. Olivetti, G. Ceder, G. G. Gaustad and X. Fu, *Joule*, 2017, **1**, 229-243.
5. N. Yabuuchi, K. Kubota, M. Dahbi and S. Komaba, *Chem. Rev.*, 2014, **114**, 11636-11682.
6. J.-Y. Hwang, S.-T. Myung and Y.-K. Sun, *Chem. Soc. Rev.*, 2017, **46**, 3529-3614.
7. M. H. Han, E. Gonzalo, G. Singh and T. Rojo, *Energy Environ. Sci.*, 2015, **8**, 81-102
8. P. Barpanda, L. Lander, S. Nishimura and A. Yamada, *Adv. Energy Mater.*, 2018, **8**, 1703055.
9. M. Dahbi, N. Yabuuchi, K. Kubota, K. Tokiwa and S. Komaba, *Phys. Chem. Chem. Phys.*, 2014, **16**, 15007-15028.
10. K. Kubota and S. Komaba, *J. Electrochem. Soc.*, 2015, **162**, A2538-A2550.
11. C. Delmas, J. J. Braconnier, C. Fouassier and P. Hagenmuller, *Solid State Ion.*, 1981, **3**, 165-169.
12. J. Zhao, L. Zhao, N. Dimov, S. Okada and T. Nishida, *J. Electrochem. Soc.*, 2013, **160**, A3077-A3081.
13. N. Yabuuchi, M. Kajiyama, J. Iwatate, H. Nishikawa, S. Hitomi, R. Okuyama, R. Usui, Y. Yamada and S. Komaba, *Nat. Mater.*, 2012, **11**, 512-517.

14. P. Barpanda, G. Oyama, S. Nishimura, S. C. Chung and A. Yamada, *Nat. Commun.*, 2014, **5**, 4358.
15. C. Vaalma, D. Buchholz, M. Weil and S. Passerini, *Nat. Rev. Mater.*, 2018, **3**, 1-11.
16. R. Rajagopalan, Y. Tang, X. Ji, C. Jia and H. Wang, *Adv. Funct. Mater.*, 2020, **30**, 1909486.
17. T. Hosaka, K. Kubota, A. Shahul Hameed and S. Komaba, *Chem. Rev.*, 2020, **120**, 6358-6466.
18. Y. Ru, S. Zheng, H. Xue and H. Pang, *J. Mater. Chem. A.*, 2019, **7**, 14391-14418.
19. D. Aurbach, Y. Gofer, Z. Lu, A. Schechter, O. Chusid, H. Gizbar, Y. Cohen, V. Ashkenazi, M. Moshkovich and R. Turgeman, *J. Power Sources*, 2001, **97**, 28-32.
20. M. M. Huie, D. C. Bock, E. S. Takeuchi, A. C. Marschilok and K. J. Takeuchi, *Coord. Chem. Rev.*, 2015, **287**, 15-27.
21. S. K. Das, S. Mahapatra and H. Lahan, *J. Mater. Chem. A*, 2017, **5**, 6347-6367.
22. M. E. Arroyo-de Dompablo, A. Ponrouch, P. Johansson and M. R. Palacin, *Chem. Rev.*, 2020, **120**, 6331-6357.
23. K. M. Abraham, *Solid State Ionics*, 1982, **7**, 199-212.
24. J. J. Braconnier, C. Delmas and P. Hagenmuller, *Mater. Res. Bull.*, 1982, **17**, 993-1000.
25. K. Mizushima, P. C. Jones, P. J. Wiseman and J. B. Goodenough, *Mater. Res. Bull.*, 1980, **15**, 783-789.
26. A. Manthiram and J. B. Goodenough, *J. Power Sources*, 1989, **26**, 403-408
27. L. X. Yuan, Z. H. Wang, W. X. Zhang, X. L. Hu, J. T. Chen, Y. H. Huang and J. B. Goodenough, *Energy Environ. Sci.*, 2011, **4**, 269-284.
28. P. Barpanda, S. Nishimura and A. Yamada, *Adv. Energy Mater.*, 2012, **2**, 841-859.
29. P. Barpanda, T. Ye, S. Nishimura, S. C. Chung, Y. Yamada, M. Okubo, H. Zhou and A. Yamada, *Electrochem. Commun.*, 2012, **24**, 116-119.
30. B. L. Ellis, W. R. M. Makahnouk, Y. Makimura, K. Toghill and L. F. Nazar, *Nat. Mater.*, 2007, **6**, 749-753.
31. L. Sharma, S. P. Adiga, H. N. Alshareef and P. Barpanda, *Adv. Energy Mater.*, 2020, **10**, 2001449.
32. G. Rousse and J. M. Tarascon, *Chem. Mater.*, 2014, **26**, 394-406.
33. P. Barpanda, *Isr. J. Chem.*, 2015, **55**, 537-557.
34. A. Nyten, A. Abouimrane, M. Armand, T. Gustafsson and J. O. Thomas, *Electrochem. Commun.*, 2005, **7**, 156-160.

35. M. S. Islam, R. Dominko, C. Masquelier, C. Sirisopanaporn, A. R. Armstrong and P. G. Bruce, *J. Mater. Chem.*, 2011, **21**, 9811-9818.
36. V. Legagneur, Y. An, A. Mosbah, R. Portal, A. Le Gal La Salle, A. Verbaere, D. Guyomard and Y. Piffard, *Solid State Ionics*, 2001, **139**, 37-46.
37. P. Barpanda, D. Dwibedi, S. Ghosh, Y. Kee and S. Okada, *Ionics*, 2015, **21**, 1801-1812.
38. C. Masquelier and L. Croguennec, *Chem. Rev.*, 2013, **113**, 6552-6591.
39. B. Senthilkumar, C. Murugesan, L. Sharma, S. Lochab and P. Barpanda, *Small Methods*., 2019, **3**, 1800253.
40. H. Chen, Q. Hao, O. Zivkovic, G. Hautier, L.-S. Du, Y. Tang, Y.-Y. Hu, X. Ma, C. P. Grey and G. Ceder, *Chem. Mater.*, 2013, **25**, 2777-2786
41. H. Kim, I. Park, D.-H. Seo, S. Lee, S.-W. Kim, W. J. Kwon, Y.-U. Park, C. S. Kim, S. Jeon and K. Kang, *J. Am. Chem. Soc.*, 2012, **134**, 10369-10372.
42. H. Kim, G. Yoon, I. Park, K.-Y. Park, B. Lee, J. Kim, Y.-U. Park, S.-K. Jung, H.-D. Lim, D. Ahn, S. Lee and K. Kang, *Energy Environ. Sci.*, 2015, **8**, 3325-3335.
43. J. Kim, G. Yoon, M. H. Lee, H. Kim, S. Lee and K. Kang, *Chem. Mater.*, 2017, **29**, 7826-7832.
44. A. J. Fernández-Ropero, M. Zarrabeitia, M. Reynaud, T. Rojo and M. Casas-Cabanas, *J. Phys. Chem. C.*, 2018, **122**, 133-142.
45. M. Law and P. Balaya, *Energy Storage Mater.*, 2018, **10**, 102-113.
46. J. Liu, D. Chang, P. Whitfield, Y. Janssen, X. Yu, Y. Zhou, J. Bai, J. Ko, K.-W. Nam and L. Wu, *Chem. Mater.*, 2014, **26**, 3295-3305.
47. Y. Lu, S. Zhang, Y. Li, L. Xue, G. Xu and X. Zhang, *J. Power Sources*, 2014, **247**, 770-777.
48. M. Nose, H. Nakayama, K. Nobuhara, H. Yamaguchi, S. Nakanishi and H. Iba, *J. Power Sources*, 2013, **234**, 175-179.
49. M. Nose, K. Nobuhara, S. Shiotani, H. Nakayama, S. Nakanishi and H. Iba, *RSC Adv.*, 2014, **4**, 9044-9047.
50. M. Nose, S. Shiotani, H. Nakayama, K. Nobuhara, S. Nakanishi and H. Iba, *Electrochem. Commun.*, 2013, **34**, 266-269.
51. M. Reynaud, A. Wizner, N. A. Katcho, L. C. Loaiza, M. Galceran, J. Carrasco, T. Rojo, M. Armand and M. Casas-Cabanas, *Electrochem. Commun.*, 2017, **84**, 14-18.
52. K. Shiva, P. Singh, W. Zhou and J. B. Goodenough, *Energy Environ. Sci.*, 2016, **9**, 3103-3106.

53. X. Wu, G. Zhong and Y. Yang, *J. Power Sources*, 2016, **327**, 666-674.
54. M. Xu, C.-J. Cheng, Q.-Q. Sun, S.-J. Bao, Y.-B. Niu, H. He, Y. Li and J. Song, *RSC Adv.*, 2015, **5**, 40065-40069.
55. W. Yao, M.-T. Sougrati, K. Hoang, J. Hui, P. Lightfoot and A. R. Armstrong, *Chem. Mater.*, 2017, **29**, 2167-2172.
56. N. Recham, J. N. Chotard, L. Dupont, C. Delacourt, W. Walker, M. Armand and J.-M. Tarascon, *Nat. Mater.*, 2010, **9**, 68-74.
57. P. Barpanda, M. Ati, B. C. Melot, G. Rousse, J. N. Chotard, M.-L. Doublet, M. T. Sougrati, S. A. Corr, J.-C. Jumas and J.-M. Tarascon, *Nat. Mater.*, 2011, **10**, 772-779.
58. M. Ati, B. C. Melot, G. Rousse, J. N. Chotard, P. Barpanda and J. M. Tarascon, *Angew. Chem. Int. Ed.*, 2011, **50**, 10574-10577.
59. P. Barpanda, N. Recham, J. N. Chotard, K. Djellab, W. Walker, M. Armand and J. M. Tarascon, *J. Mater. Chem.*, 2010, **20**, 1659.
60. W. Baur, *Acta Crystallogr.*, 1959, **12**, 988-994.
61. V. I. Simonov and N. V. Belov, *J. Sov. Phys. Crystallogr.*, 1958, **3**, 429-438.
62. N. Marx, L. Croguennec, D. Carlier, A. Wattiaux, F. Le Cras, E. Suard and C. Delmas, *Dalton Trans.*, 2010, **39**, 5108-5116.
63. S. Yang, Y. Song, P. Y. Zavalij and M. S. Whittingham, *Electrochem. Commun.*, 2002, **4**, 239-244.
64. H. Y. Asl and A. Choudhury, *RSC Adv.*, 2014, **4**, 37691-37700.
65. B. L. Ellis, T. N. Ramesh, W. N. Rowan-Weetaluktuk, D. H. Ryan and L. F. Nazar, *J. Mater. Chem.*, 2012, **22**, 4759-4766.
66. L. Sharma, K. Nakamoto, S. Okada and P. Barpanda, *J. Power Sources* 2019, **429**, 17-21.
67. L. Sharma, S. Bharathraj, P. Barpanda, S. P. Adiga and K. S. Mayya, *ACS Appl. Energy Mater.* 2021, **4**, 1021-1032.
68. N. Marx, L. Croguennec, D. Carlier, L. Bourgeois, P. Kubiak, F. L. Cras and C. Delmas, *Chem. Mater.*, 2010, **22**, 1854-1861.
69. A. Castets, D. Carlier, Y. Zhang, F. Boucher, N. Marx, L. Croguennec and M. Ménétrier, *J. Phys. Chem. C.*, 2011, **115**, 16234-16241.
70. M. A. G. Aranda, S. Bruque, J. P. Attfield, F. Palacio and R. B. V. Dreele, *J. Solid State Chem.*, 1997, **132**, 202-212.
71. Y. Yang, M. Hirayama, M. Yonemura and R. Kanno, *J. Solid State Chem.*, 2012, **187**, 124-129.

72. Y. Yang, M. Hirayama, K. Kubota and R. Kanno, *J. Power Sources*, 2012, **205**, 394-401.
73. A. Castets, D. Carlier, Y. Zhang, F. Boucher, N. Marx, R. Gautier, E. Le Fur, L. Le Pollès, L. Croguennec and M. Ménétrier, *Solid State Nucl. Magn. Reson.*, 2012, **42**, 42-50.
74. E. Boivin, J.-N. Chotard, M. Ménétrier, L. Bourgeois, T. Bamine, D. Carlier, F. Fauth, E. Suard, C. Masquelier and L. Croguennec, *J. Mater. Chem. A.*, 2016, **4**, 11030-11045.
75. M. A. Reddy, V. Pralong, V. Caignaert, U. V. Varadaraju and B. Raveau, *Electrochem. Commun.*, 2009, **11**, 1807-1810.
76. M. Ati, M. T. Sougrati, G. Rousse, N. Recham, M. L. Doublet, J. C. Jumas and J.-M. Tarascon, *Chem. Mater.*, 2012, **24**, 1472-1485.
77. X.-M. Liu, S.-L. Zhang, M. Yang, X.-Z. Liao, H. Yang, X.-D. Shen and Z.-F. Ma, *Chem. Comm.*, 2014, **50**, 15247-15250.
78. C. V. Subban, M. Ati, G. Rousse, A. M. Abakumov, G. V. Tendeloo, R. Janot and J.-M. Tarascon, *J. Am. Chem. Soc.*, 2013, **135**, 3653-3661.
79. C. Eames, J. M. Clark, G. Rousse, J.-M. Tarascon and M. S. Islam, *Chem. Mater.*, 2014, **26**, 3672-3678.
80. F. W. Badrudin, M. F. M. Taib, O. H. Hassan and M. Z. A. Yahya, *Comput. Mater. Sci.*, 2016, **119**, 144-151.
81. F. W. Badrudin, M. F. M. Taib, R. I. P. R. Mustapha, O. H. Hassan and M. Z. A. Yahya, *Mater. Today. Proc.*, 2017, **4**, 5108-5115.
82. A. V. Radha, C. V. Subban, M. L. Sun, J.-M. Tarascon and A. Navrotsky, *J. Mater. Chem. A*, 2014, **2**, 6887-6894.
83. A. H. Reshak and W. Khan, *J. Alloys Compd.*, 2014, **591**, 362-369.
84. L. Zhang, J.-M. Tarascon, M. T. Sougrati, G. Rousse and G. Chen, *J. Mater. Chem. A*, 2015, **3**, 16988-16997.
85. G. A. Swayze, G. A. Desborough, K. S. Smith, H. A. Lowers, J. M. Hammarstrom, S. F. Diehl, R. W. Leinz, R. L. Driscoll and P. L. Verplanck, *Circ. U.S. Geol. Surv.*, 2008, **1328**, 8-13.
86. M. E. Elwood Madden, R. J. Bodnar and J. D. Rimstidt, *Nature*, 2004, **431**, 821-823.
87. R. G. Burns, *Nature*, 1986, **320**, 55-56.
88. P. R. Christensen, M. B. Wyatt, T. D. Glotch, A. D. Rogers, S. Anwar, R. E. Arvidson, J. L. Bandfield, D. L. Blaney, C. Budney, W. M. Calvin, A. Fallacaro, R. L.

Fergason, N. Gorelick, T. G. Graff, V. E. Hamilton, A. G. Hayes, J. R. Johnson, A. T. Knudson, H. Y. McSween, G. L. Mehall, L. K. Mehall, J. E. Moersch, R. V. Morris, M. D. Smith, S. W. Squyres, S. W. Ruff and M. J. Wolff, *Science*, 2004, **306**, 1733-1739.

89. A. Navrotsky, F. L. Forray and C. Drouet, *Icarus*, 2005, **176**, 250-253.
90. S. J. Mills, F. Nestola, V. Kahlenberg, A. G. Christy, C. Hejny and G. J. Redhammer, *Am. Mineral.*, 2013, **98**, 1966-1971.
91. S. B. Hendricks, *Am. Mineral.*, 1937, **22**, 773-784.
92. J. L. Jambor, *Canad. Mineral.*, 1999, **37**, 1323-1341.
93. A. S. Wills and A. Harrison, *J. Chem. Soc., Faraday Trans.*, 1996, **92**, 2161-2166.
94. J. Dutrizac, *Metall. Trans. B*, 1983, **14**, 531-539.
95. D. Grohol and D. G. Nocera, *J. Am. Chem. Soc.*, 2002, **124**, 2640-2646.
96. J. B. Goodenough, *J. Phys. Chem. Solids*, 1958, **6**, 287-297.
97. J. Kanamori, *J. Phys. Chem. Solids*, 1959, **10**, 87-98.
98. T. Moriya, *Phys. Rev. Lett.*, 1960, **4**, 228-230.
99. T. Moriya, *Phys. Rev.*, 1960, **120**, 91-98.
100. M. Takano, T. Shinjo, M. Kiyama and T. Takada, *J. Phys. Soc. Japan*, 1968, **25**, 902-902.
101. T. Inami, M. Nishiyama, S. Maegawa and Y. Oka, *Phys. Rev. B*, 2000, **61**, 12181-12186.
102. D. G. Nocera, B. M. Bartlett, D. Grohol, D. Papoutsakis and M. P. Shores, *Chem. Eur. J.*, 2004, **10**, 3850-3859.
103. D. Papoutsakis, D. Grohol and D. G. Nocera, *J. Am. Chem. Soc.*, 2002, **124**, 2647-2656.
104. R. A. Klein, J. P. S. Walsh, S. M. Clarke, Y. Guo, W. Bi, G. Fabbris, Y. Meng, D. Haskel, E. E. Alp, R. P. Van Duyne, S. D. Jacobsen and D. E. Freedman, *J. Am. Chem. Soc.*, 2018, **140**, 12001-12009.
105. M. Gnanavel, V. Pralong, O. I. Lebedev, V. Caignaert, P. Bazin and B. Raveau, *Chem. Mater.*, 2014, **26**, 4521-4527.
106. M. Gnanavel, O. I. Lebedev, P. Bazin, B. Raveau and V. Pralong, *Solid State Ion.*, 2015, **278**, 38-42.
107. N. V. Kosova, A. A. Shindrov and A. A. Kabanov, *Electrochim. Acta*, 2020, **359**, 136950-136961.

108. Y.-L. Ding, Y. Wen, P. A. van Aken, J. Maier and Y. Yu, *Chem. Mater.*, 2015, **27**, 3143-3149.
109. Y.-L. Ding, Y. Wen, C.-C. Chen, P. A. van Aken, J. Maier and Y. Yu, *ACS Appl. Mater. & Interfaces*, 2015, **7**, 10518-10524.
110. W. Xu, Z. Xie, X. Cui, K. Zhao, L. Zhang, L. Mai and Y. Wang, *J. Mater. Chem. A*, 2016, **4**, 3735-3742.
111. R. Zhao, Y. Li and C. K. Chan, *J. Phys. Chem. C*, 2016, **120**, 9702-9712.
112. Z. G. Neale, M. Barta and G. Cao, *ACS Appl. Energy Mater.*, 2021, **4**, 2248-2256.
113. F. Wang, S. Liu, Q. Jiang, K. Feng, X. Yang, X. Li, H. Zhang, M. Xia and H. Zhang, *J. Power Sources*, 2020, **452**, 227835-227842.
114. R. Miyawaki, F. Hatert, M. Pasero and S. J. Mills, *Eur. J. Mineral.*, 2020, **32**, 1-11.
115. R. L. Frost, R. Scholz, F. M. Belotti, A. López, F. L. Theiss and B. Spectroscopy, *Spectrochimica Acta Part A: Molecular*, 2015, **147**, 185-192.
116. R. L. Frost, Y. Xi, R. Scholz, A. López, R. M. F. Lima and C. M. Ferreira, *Vib. Spectrosc.*, 2013, **67**, 14-21.
117. J. M. Hughes and J. Rakovan, *Rev Mineral Geochem*, 2002, **48**, 1-12.
118. P. Sandineni, H. Yaghoobnejad Asl and A. Choudhury, *J. Solid State Chem.*, 2016, **242**, 78-86.
119. B. M. Bartlett and D. G. Nocera, *J. Am. Chem. Soc.*, 2005, **127**, 8985-8993.
120. K. Momma, F. Izumi, *J. Appl. Crystallogr.*, 2011, **44**, 1272-1276.

**Table 1.** Overview of hydroxyphosphate-based cathode materials for Li-ion batteries.

| **Materials (Formulae)** | **Structure** | **Redox Species** | **Redox Potential** | **Rate** | **Capacity (mAh.g$^{-1}$)** (Observed/ Theoretical) | **References** |
|---|---|---|---|---|---|---|
| $LiFePO_4OH$ | *Tavorite* triclinic ($P\bar{1}$) | $Fe^{+3}/Fe^{+2}$ | 2.6 V | 1.0 mA cm$^{-2}$ | 140/ 153 | 66 |
| | | $Fe^{+3}/Fe^{+2}$ | 2.6-2.7 V | 1.0 mA cm$^{-2}$ (aqueous) | 153/153 | |
| $LiMnPO_4OH$ | *Tavorite* triclinic ($P\bar{1}$) | $Mn^{+4}/Mn^{+3}$ | 3.4 V | C/100 | 110/ 154 | 71 |
| $LiVPO_4OH$ | *Tavorite* triclinic ($P\bar{1}$) | $V^{+4}/V^{+3}$ | 3.95 V | C/100 | 280/ 158 | 74 |
| | | $V^{+3}/V^{+2}$ | 1.4 V | C/100 | 136/ 158 | |

**Table 2.** Naturally occuring hydroxyphosphate-based minerals with potential application in design of battery insertion materials.[112-116]

| Mineral name | Chemical Formulae |
|---|---|
| Whitetite | $CaMn^{++}Mg_2Al_2(PO_4)_4(OH)_2.8H_2O$ |
| Vantasselite | $Al_4(PO_4)_3(OH)_3.9H_2O$ |
| Apatite | $Ca_5(PO_4)_3(F,OH,Cl)$ |
| Leucophosphite | $K_2[Fe_4(OH)_2(H_2O)_2(PO_4)_4].2H_2O$ |
| Nordgauite | $MnAl_2(PO_4)_2(F,OH)_2.5H_2O$ |
| Skorpionite | $Ca_3Zn_2(PO_4)_2CO_3(OH)_2.H_2O$ |
| Metavivianite | $Fe^{+2}Fe_2^{+3}(PO_4)_2(OH)_2.6H_2O$ |
| Trolleite | $Al_4(OH_3)[PO_4]_3$ |
| Weinebeneite | $CaBe_3(PO_4)_2(OH)_2.4H_2O$ |
| Hentschelite | $CuFe_2(PO_4)_2(OH)_2$ |
| Kastningite | $(Mn,Fe,Mg)(H_2O)_4[Al_2(OH)_2(H_2O)_2(PO_4)_2].2H_2O$ |
| Phosphuranylite | $Ca(UO_2)[(UO_2)_3(OH)_2(PO_4)_2]_2.12H_2O$ |
| Plimerite | $ZnFe_4(PO_4)_3(OH)_5$ |
| Paravauxite | $FeAl_2(PO_4)_2(OH)_2.8H_2O$ |
| Tvrdyite | $Fe^{+2}Fe_2^{+3}Al_3(PO_4)_4(OH)_5(OH)_5(OH_2)_4.2H_2O$ |
| Hydroxylpyromorphite | $Pb_{10}(PO_4)_6(OH_2)$ |
| Rockbridgeite | $Fe_{4.32}Mn_{0.62}Zn0_{.06}(PO_4)_3(OH)_5$ |
| Lakebogaite | $CaNaFe_2^{+3}H(UO_2)_2(PO_4)_4(OH)_2(H_2O)_8$ |
| Jahnsite | $Mn^{+2}Mn^{+2}Fe^{+3}{}_2Fe^{+3}{}_2(PO_4)_4(OH)_2.8H_2O$ |
| Foggite | $CaAl(PO_4)(OH)_2.H_2O$ |
| Vendidaite | $Al_2(SO_4)(OH)_3Cl(H_2O)_6$ |
| Girvasite | $NaCa_2Mg_3(PO_4)_4(CO_3)(H_2O)_6$ |
| Meurigite | $[Na(H_2O)_{2.5}][Fe^{3+}{}_8(PO_4)_6(OH)_7(H_2O)_4]$ |
| Whitmoreite | $CuFe^{3+}{}_2(PO_4)_2(OH)_2{\cdot}4H_2O$ |
| Eosphorite-Childrenite | $(Mn,Fe)Al(PO_4)(OH)_2{\cdot}H_2O$ |
| Melonjosephite | $Ca_2[(Fe^{+2}{}_{0.5}FeO^{+3}{}_{0.5})_4(OH)_2(PO_4)_4]$ |

**Table 3.** Overview of hydroxysulfate-based cathode materials for Li-ion batteries.

| **Materials (Formulae)** | **Structure** | **Redox Species** | **Redox Potential** | **Rate** | **Capacity ($mAh.g^{-1}$)** (Observed/ Theoretical) | **References** |
|---|---|---|---|---|---|---|
| $LiFeSO_4OH$ | Layered monoclinic ($P2_1/c$) | $Fe^{+3}/Fe^{+2}$ | 3.6 V | C/20 | 110/159 | 78 |
| $FeSO_4OH$ | *Tavorite* monoclinic ($P2_1/c$) | $Fe^{+3}/Fe^{+2}$ | 3.2 V | C/20 | 110/159 | 75 |
| $LiMnSO_4OH$ | Layered monoclinic ($P2_1/c$) | -- | -- | -- | --/153.19 | 78 |
| $LiCoSO_4OH$ | Layered monoclinic ($P2_1/c$) | $Co^{+3}/Co^{+2}$ | 4.7 V | -- | ~30/149.77 | 78 |
| $LiNiSO_4OH$ | Layered monoclinic ($P2_1/c$) | -- | -- | -- | --/149.97 | 78 |

**Table 4.** *Alunite* supergroup of minerals encompassing jarosites as a subclass of minerals.[90]

| Name | Composition |
|---|---|
| Sulfates | |
| Alunite | $KAl_3(SO_4)_2(OH)_6$ |
| Natroalunite | $NaAl_3(SO_4)_2(OH)_6$ |
| Harttite | $SrAl_3(SO_4)_2(OH)_6$ |
| Jarosite | $KFe_3(SO_4)_2(OH)_6$ |
| Natrojarosite | $NaFe_3(SO_4)_2(OH)_6$ |
| Hydronium-jarosite | $(H_3O)Fe_3(SO_4)_2(OH)_6$ |
| Argento-jarosite | $AgFe_3(SO_4)_2(OH)_6$ |
| Ammonio-jarosite | $NH_4Fe_3(SO_4)_2(OH)_6$ |
| Plumbo-jarosite | $Pb_{1/2}Fe_3(SO_4)_2(OH)_6$ |
| Beaverite | $PbCu(FeAl)_2(SO_4)_2(OH)_6$ |
| Phosphates | |
| Hamlinite | $SrAl_3(PO_4)_2(OH)_5.H_2O$ |
| Plumbogummite | $PbAl_3(PO_4)_2(OH)_5.H_2O$ |
| Gorceixite | $BaAl_3(PO_4)_2(OH)_5.H_2O$ |
| Florencite | $Ce_{5/6}Al_3(PO_4)_2(OH)_5.H_2O$ |
| Mixed | |
| Beudantite | $PbFe_3(AsO_4)(SO_4)(OH)_6$ |
| Corkite | $PbFe_3(PO_4)(SO_4)(OH)_6$ |
| Savanbergite | $SrAl_3(AsO_4)(SO_4)(OH)_6$ |
| Hinsdalite | $PbAl_3(PO_4)(SO_4)(OH)_6$ |

**Table 5.** Jarosites as electrode materials for metal-ion insertion batteries.

| Compounds | *vs.* | Activity | Redox Species | Rate | Capacity (mAh/g) | Reference |
|---|---|---|---|---|---|---|
| ***as cathode*** | | | | | | |
| $NaFe_3(SO_4)_2(OH)_6$ *Precipitation route* | $Li^+/Li$ | 2.82 V | $Fe^{3+}/Fe^{2+}$ | C/20 | 120/166 | 104 |
| | $Na^+/Na$ | 2.72 V | $Fe^{3+}/Fe^{2+}$ | C/20 | 120/166 | 105 |
| $NaFe_3(SO_4)_2(OH)_6$ *Hydrothermal synthesis* | $Li^+/Li$ | 2.71/2.63 V 3.03/2.93 V | $Fe^{3+}/Fe^{2+}$ | C/20 | 71/166 | 106 |
| | $Na^+/Na$ | 2.55 V | $Fe^{3+}/Fe^{2+}$ | C/20 | 80/166 | |
| $KFe_3(SO_4)_2(OH)_6$ *Template-assisted redox coprecipitation* | $Li^+/Li$ | 2.09/1.85 V 2.87/2.42 V | $Fe^{3+}/Fe^{2+}$ | C/5 | 117/160 | 107 |
| | $Na^+/Na$ | | $Fe^{3+}/Fe^{2+}$ | C/10 | ~115/160 | |
| $KFe_3(SO_4)_2(OH)_6$/rGO composite | $Li^+/Li$ | 2.31/2.58 V | $Fe^{3+}/Fe^{2+}$ | 1C | 143.6/160 | 109 |
| $NH_4Fe_3(SO_4)_2(OH)_6$ *Hydrothermal route* | $Li^+/Li$ | | $Fe^{3+}/Fe^{2+}$ | C/20 | ~ 30/168 | 117 |
| $NaFe_3(SO_4)_2(OH)_{6-x}F_x$ x= 0.34 *Precipitation route* | $Li^+/Li$ | | $Fe^{3+}/Fe^{2+}$ | C/20 | ~ 105 | 117 |
| $Na_{1-x}(H_3O)_xV_3(SO_4)_2(OH)_6$ x = 0.048 *microwave assisted hydrothermal reaction* | $Li^+/Li$ | 1.1/1.3 V 1.4/1.6 V | $V^{3+}/V^{2+}$ | | ~63/171 | 110 |
| | $Na^+/Na$ | | $V^{3+}/V^{2+}$ | | ~3 | |
| $K_{1-x}(H_3O)_xV_3(SO_4)_2(OH)_6$ x = 0.014 *microwave assisted hydrothermal reaction* | $Li^+/Li$ | | $V^{3+}/V^{2+}$ | | ~40 | |
| $Pb_{0.5}Fe_3(SO_4)_2(OH)_6$ | $Na^+/Na$ | 2.3, 2.5/2.6V | $Fe^3/Fe^{2+}$ | C/5 | 91.4/142 | 111 |
| **Non-Jarosite** | | | | | | |
| $K_2Fe_3(SO_4)_3(OH)_2(H_2O)_2$ Hydrothermal route | $Li^+/Li$ | 2.5/2.2 V 3.2/3.0 V | $Fe^{2+}/Fe^{3+}$ | C/5 | 120/100 | 111 |
| | $Na^+/Na$ | 3.1/2.6 V | $Fe^{2+}/Fe^{3+}$ | C/5 | 110/100 | |
| | $K^+/K$ | 3.3/2.8 V | $Fe^{2+}/Fe^{3+}$ | C/5 | 100/100 | |
| ***as anode*** | | | | | | |
| $NaFe_3(SO_4)_2(OH)_6$ | $Li^+/Li$ | | $Fe^{3+}/Fe^0$ | | 516 | 110 |
| $KFe_3(SO_4)_2(OH)_6$ *Template-assisted redox coprecipitation* | $Li^+/Li$ | | $Fe^{3+}/Fe^0$ | 100 mA/g | ~1250 | 108 |

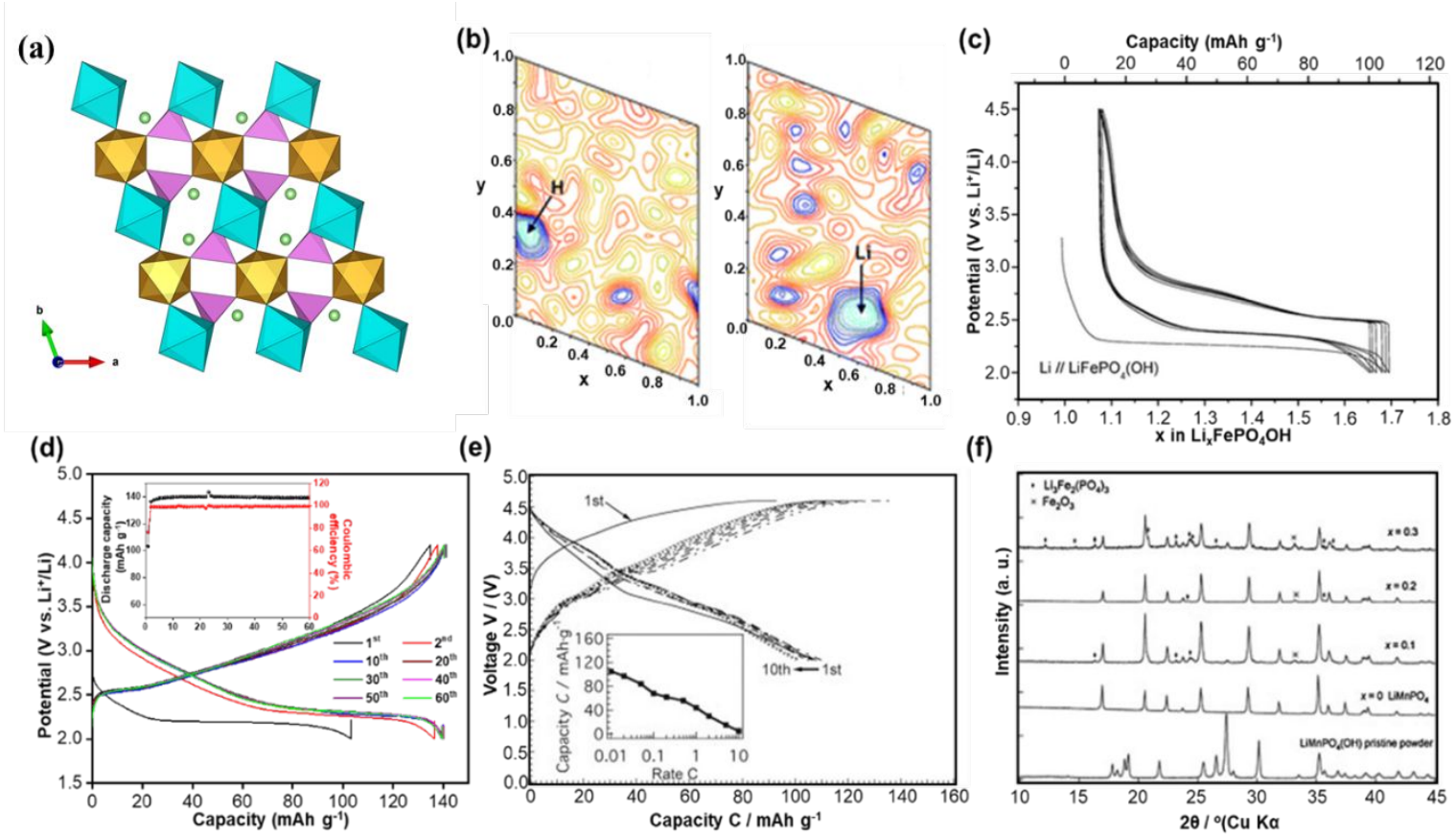


**Figure 1**. (a) Crystal structure of $LiFePO_4OH$. The iron octahedra ($FeO_6$) are shown in blue and brown colour while the phosphate tetrahedra ($PO_4$) are shown in pink color. (b) Fourier maps to determine the position of H and Li in $LiFePO_4OH$. (c) First reported lithium (de)intercalation profile of $LiFePO_4OH$. (d) The (dis)charge profile showing a stable discharge capacity of 140 mAh $g^{-1}$ upto 60 cycles. (e) (Dis)charge profile of $LiMnPO_4OH$ as a cathode for lithium-ion batteries. f) Powder X-ray diffraction patterns recorded at different composition of $LiMn_{1-x}Fe_xPO_4OH$. (b, c) Reproduced with permission.[62] Copyright 2010, Royal Society of Chemistry. (d) Reproduced with permission.[66] Copyright 2019, Elsevier. (e) Reproduced with permission.[71] Copyright 2012, Elsevier. (f) Reproduced with permission.[72] Copyright 2012, Elsevier.

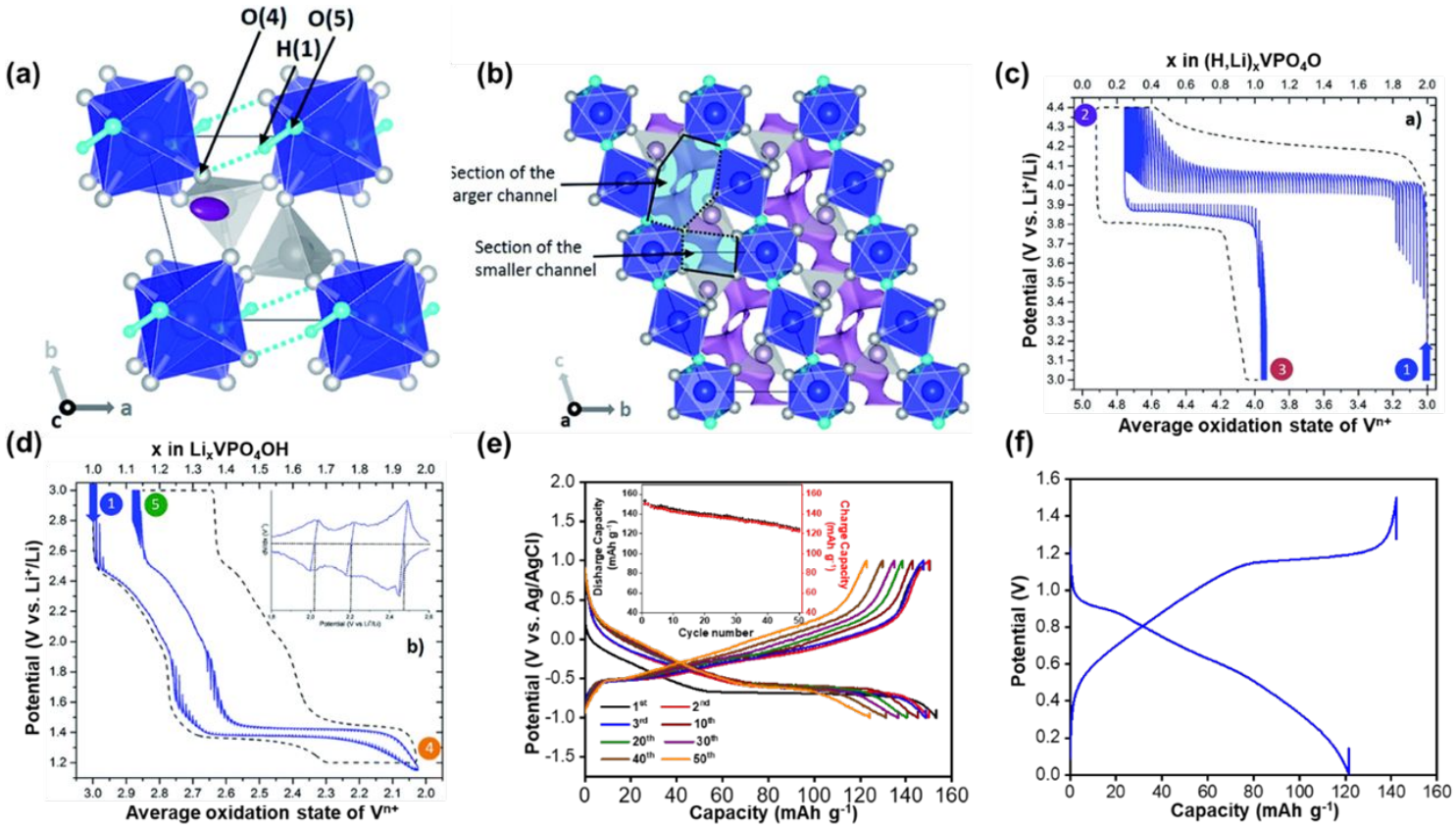


**Figure 2**. (a) Crystal structure of $LiVPO_4OH$ showing the presence of O-H as the bridging bond between two octahedra. (b) Bond valence sum Li-ion diffusion pathway analysis. (c) Galavanostatic (dis)charge properties of $LiVPO_4OH$ when cycled between 3.0 to 4.6 V (*vs.* Li). (d) Galavanostatic (dis)charge properties of $LiVPO_4OH$ when cycled between 2.0 to 1.2 V (*vs.* Li) showing the utilization of multiple oxidation state of vanadium. (e) (Dis)charge profile of $LiFePO_4OH$ in 21m LiTFSi + 7m LiOTf aqueous electrolyte when cycled between -1.0 to 1.0 V *vs.* Ag/AgCl for 50 cycles. (f) First (dis)charge curve of $LiFePO_4$|$LiFePO_4OH$ full cell in 21m LiTFSi + 7m LiOTf aqueous electrolyte having a discharge capacity of 120 mAh $g^{-1}$ at 0.8 V. (a, b, c) Reproduced with permission.[74] Copyright 2016, Royal Society of Chemitsry. (d, e) Reproduced with permission.[66] Copyright 2019, Elsevier.

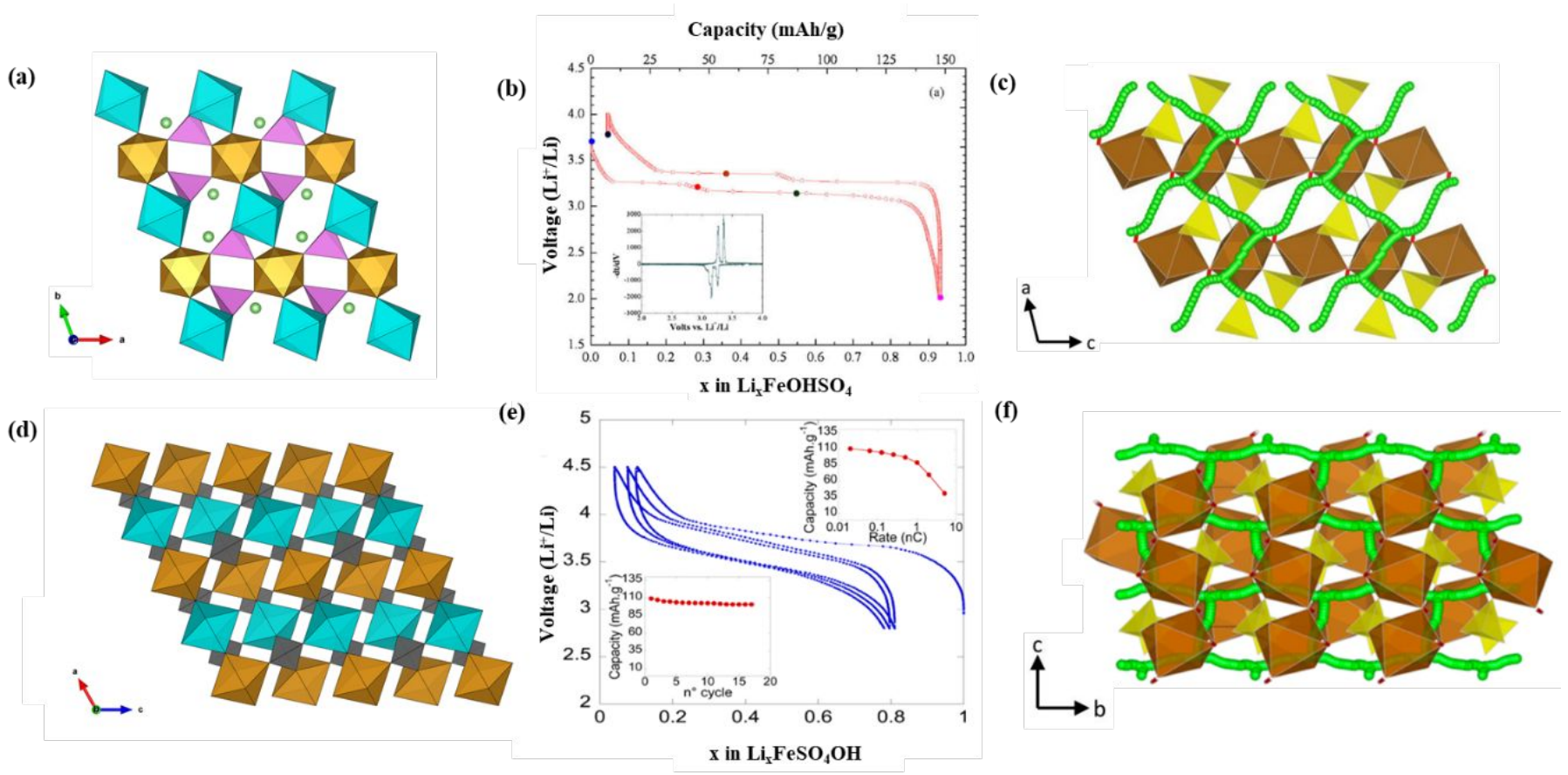


**Figure 3.** Structural illustration of (a) *tavorite* and (d) layered polymorphs of $LiFeSO_4OH$ built from interconnected $FeO_6$ octahedra (blue and brown) and $SO_4$ tetrahedra (pink or grey). Galvanostatic charge-discharge profiles of (b) *tavorite* and (e) layered $FeSO_4OH$ polymorphs. Calculated low energy pathways (c) in *tavorite* $LiFeSO_4OH$ shown along b- and c- axis (activation energy $\leq 0.72$ eV) and (f) in layered $LiFeSO_4OH$ shown along a- and c- axis (activation energy $\leq 0.19$ eV) for long range $Li^+$ ion migration. (b) Reproduced with permission.[75] Copyright 2009, Elsevier. (e) Reproduced with permission.[78] Copyright 2013, American Chemical Society(c, f) Reproduced with permission.[79] Copyright 2014, American Chemical Society.

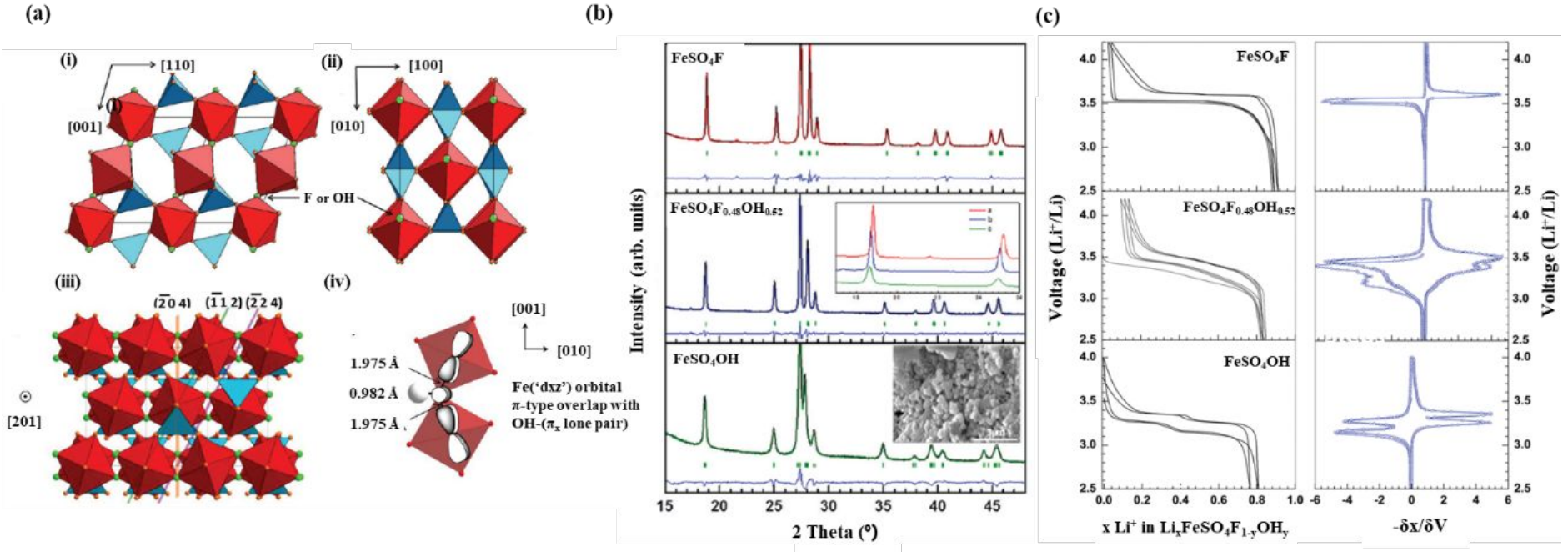


**Figure 4.** (a) Structure of $FeSO_4F_{1-y}OH_y$ (i) View along [-110]. $FeO_4(F,OH)_2$ octahedra (in red) are linked through F/OH atoms (in green) forming chains along the [001] direction. $SO_4$ tetrahedra (in blue) joining adjacent chains. (ii) View along [001] direction i.e. perpendicular to the chains. The adjacent octahedra splits away along the chains. (iii) View along the [201] direction. Traces of the (-2 0 4), (-1 1 2), and (-2 2 4) planes are represented. (iv) π-conjugation of the $OH^-$ lone pair (H atom light gray) with the $d_{xz}$ orbitals of $Fe^{3+}$ of the transition metal in the Fe-O(H)-Fe "trigonal" planar geometry. (b) Rietveld refinements of X-ray powder patterns of $FeSO_4F$, $FeSO_4F_{1-y}OH_y$ (with y = 0.55) and $FeSO_4OH$, diffraction peaks shift shown in the inset and an example of SEM image is given in the bottom. (c) Electrochemical voltage profiles for Li/$FeSO_4F$ (top), Li/$FeSO_4F_{1-y}OH_y$ (with y = 0.52) (middle) and Li/$FeSO_4OH$ cells (bottom) cycled at C/20 (left) along with the corresponding derivative curves (right). Reproduced with permission.[76] Copyright 2012, American Chemical Society.

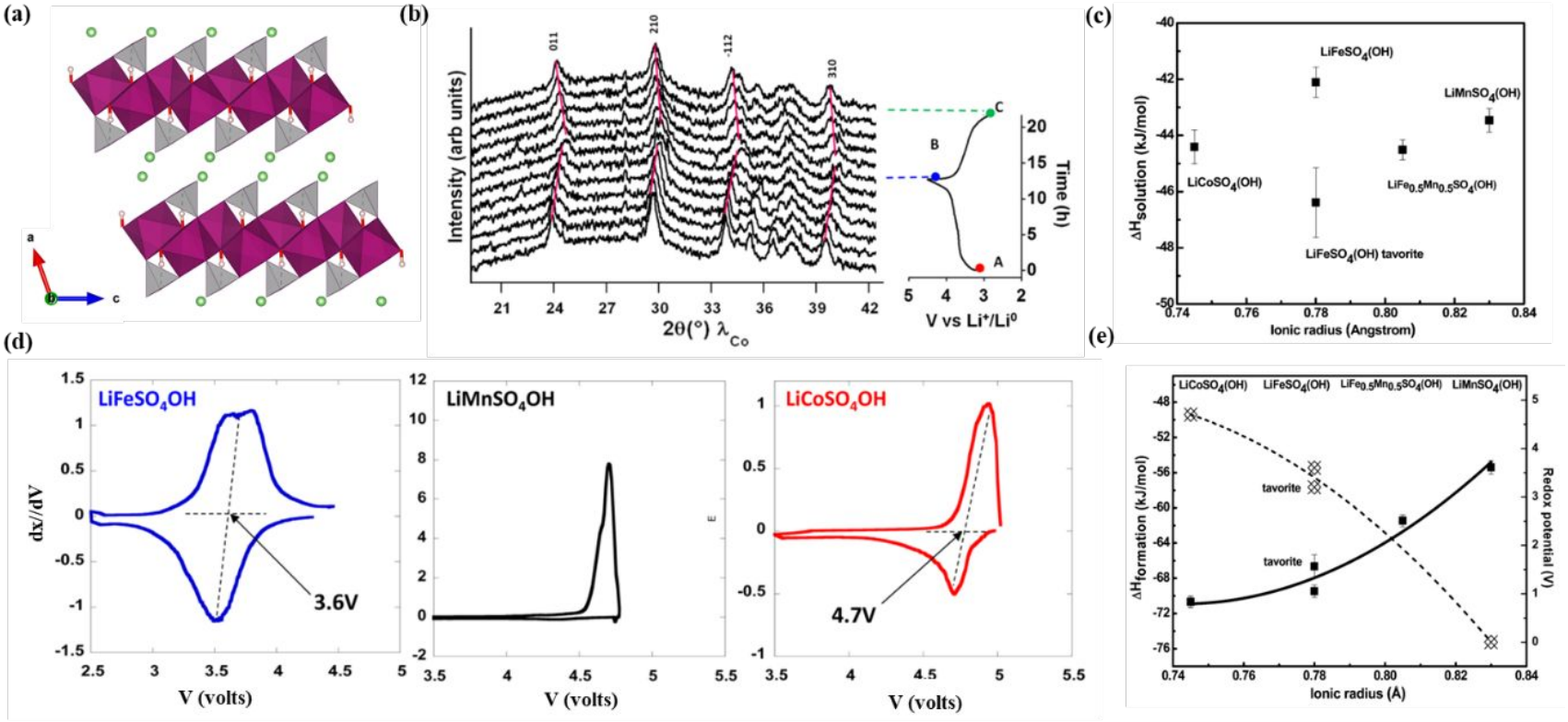


**Figure 5.** Structure and electrochemical properties of layered hydroxysulfates $LiMSO_4OH$ (M=Fe, Mn, Co). (a) Structure built with $MO_6$ octahedra (maroon) and $SO_4$ tetrahedra (grey) delimiting voids for Li atoms (green spehere). (b) *In-situ* XRD patterns of layered $LiFeSO_4OH$. (c) enthalpy of dissolution of $LiMSO_4OH$ compounds in 5 M HCl at $25^0$ C. (d) Derivative curves showing the respective redox potential. (e) enthalpies of formation (solid curve with square symbols) along with redox potentials (dashed lines with diamond symbols) as a function of cation radius. (b),(d) Reproduced with permission.[78] Copyright 2013, American Chemical Society (c), (e) Reproduced with permission.[82] Copyright 2014, The Royal Society of Chemistry.

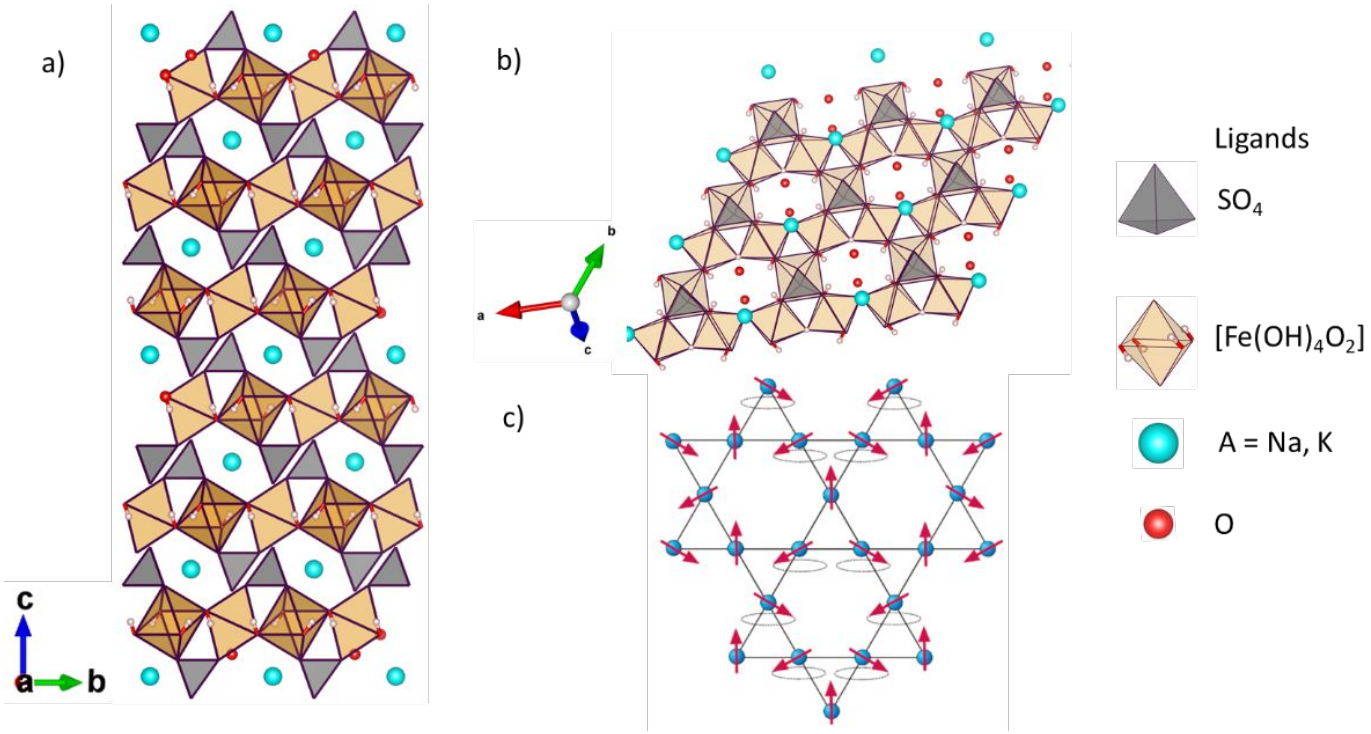


**Figure 6.** (a) Projected crystal structure of jarosite $KFe_3(SO_4)_2(OH)_6$ family along a-axis. Here, K site can accommodate monovalent $Na^+$, $Rb^+$, $Tl^+$, $NH_4^+$, $H_3O^+$ and divalent 0.5 $Pb^{2+}$, 0.5 $Hg^{2+}$ and Fe site can be substituted by $V^{3+}$, $Cr^{3+}$, $Al^{3+}$, $Ga^{3+}$, $In^{3+}$ etc. The sulfate group can be replaced by $SeO_4^{2-}$, $CrO_4^{2-}$polyanions ($SO_4$ tetrahedra, grey; $[Fe(OH)_4O_2]$ octahedra, mustard yellow; Red sphere, Oxygen; Cyan sphere, Na/K atoms). (b) Illustration of 2D layers in jarosites, which are stacked along c-axis. The layers are also known as *Kagomé* lattice. (c) Schematic representation of *Kagomé* lattice in one of the many possible ground-state degenerate configurations. (a,b) Copyright 1937. Mineralogical Society of America[90]. (c) Copyright 2014, American Chemical Society.[118]

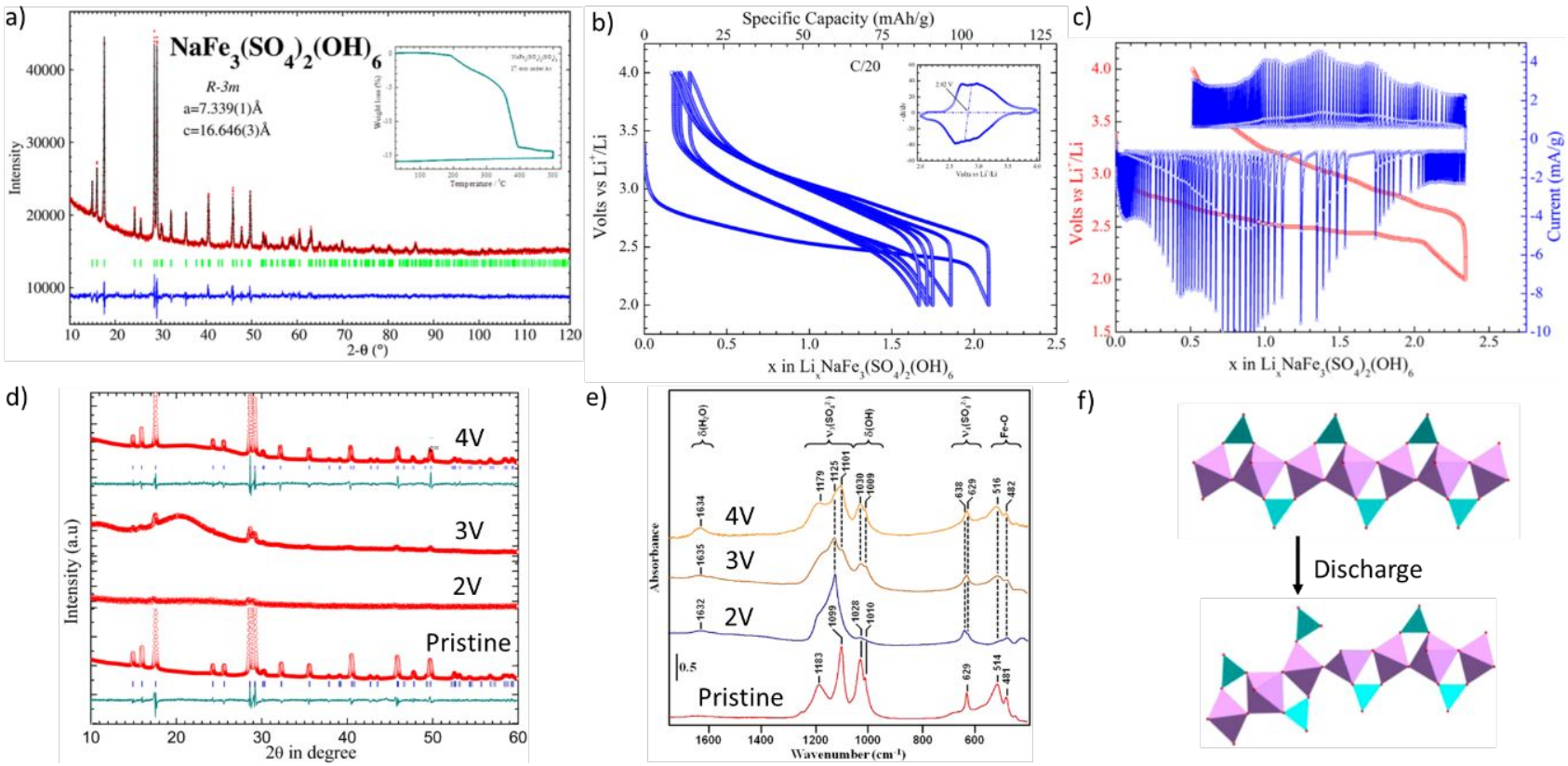


**Figure 7**. (a) Rietveld refined XRD pattern of natrojarosite, $NaFe_3(SO_4)_2(OH)_6$. (b) Galvanostatic charge-discharge curves recorded at current rate of C/20. Dramatic change can be noted between first discharge and first charge. (c) The PITT charge and discharge profile indicating change in the reaction mechanism from biphasic to topotactic in first cycle. (d) Ex situ XRD pattern comparison of pristine cathode, 2V (discharge), 3V (intermediate) and 4V (charge) state. (e) Comparative ex situ FTIR spectra of pristine cathode, 2V (discharge), 3V (intermediate) and 4V (charge). (f) Schematic representation of polyhedral distortion and defects generated at the end of first discharge. Reproduced with permission.[104] Copyright 2014, American Chemical Society.

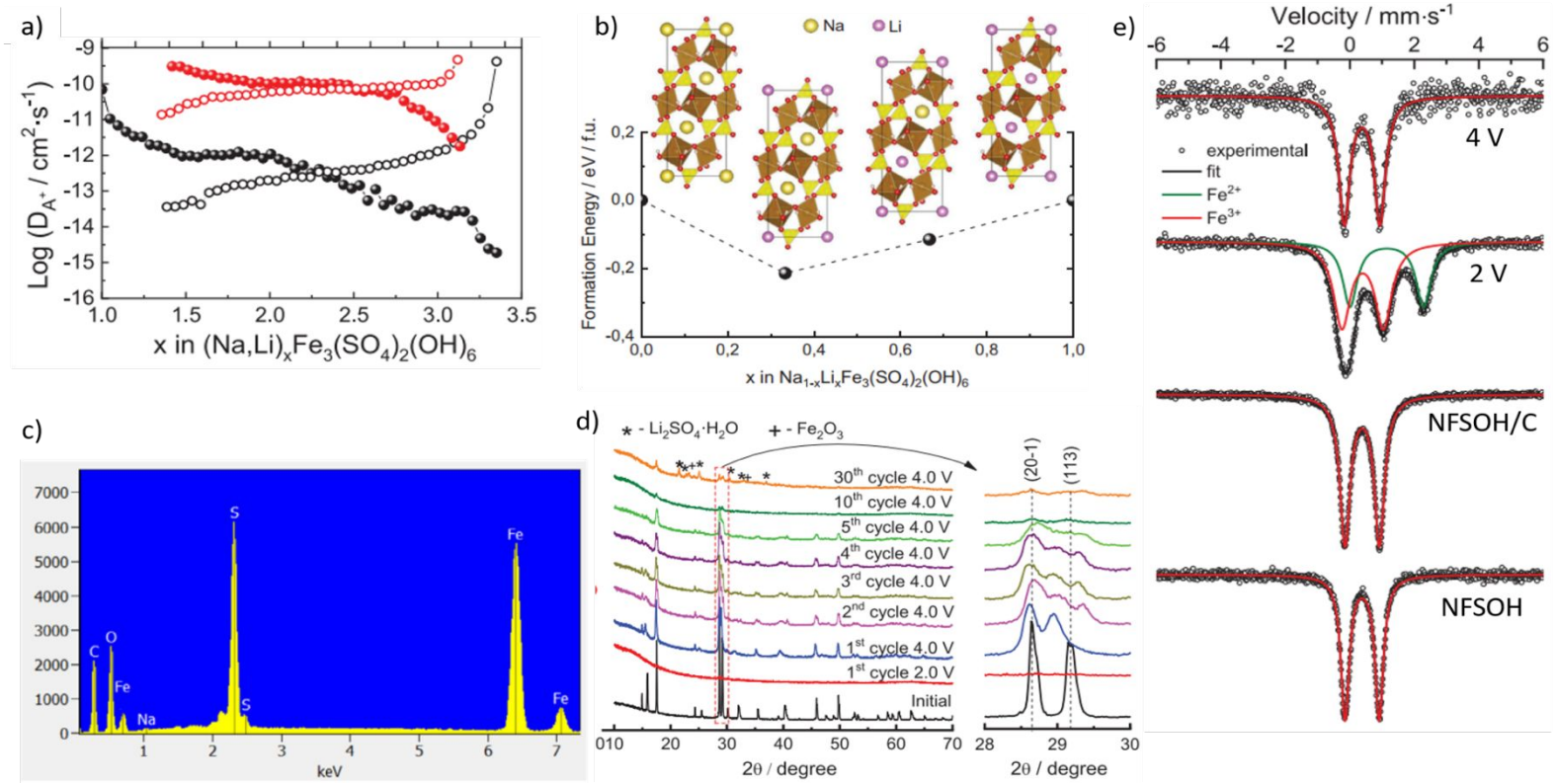


**Figure 8**. (a) Coefficient of diffusion $D_{A^+}$ ($A^+$=$Li^+$, $Na^+$) calculated from GITT plot at different value of x [$(Na,Li)_xFe_3(SO_4)_2(OH)_6$] during 1st (black sphere/circle) and 2nd cycle (red sphere/circle). (b) Formation energy estimated using DFT calculations for different values of x in $Na_{1-x}Li_xFe_3(SO_4)_2(OH)_6$. (c) Evidence of substitution of structural $Na^+$ with $Li^+$ is observed on comparison of EDS spectra of pristine NFSOH/C composite (see reference) and after 10th charge. Minor peak at ~ 1 keV indicate low amount of Na atoms in NFSOH crystal structure. (d) Ex situ XRD pattern comparison during 1st cycle, 2nd charge, 3rd charge, 4th charge, 10th charge and 30th charge. (e) $^{57}Fe$ Mössbauer spectra of pristine natrojarosite, NFSOH ($NaFe_3(SO_4)_2(OH)_6$), NFSOH/C composite, NFSOH/C composite at 1st discharge (2 V) and NFSOH/C composite at 1st charge (4 V). A constant isomer shift value of 0.38 mm.s$^{-1}$ is reported across four samples. Reproduced with permission.[106] Copyright 2020, Elsevier Ltd.

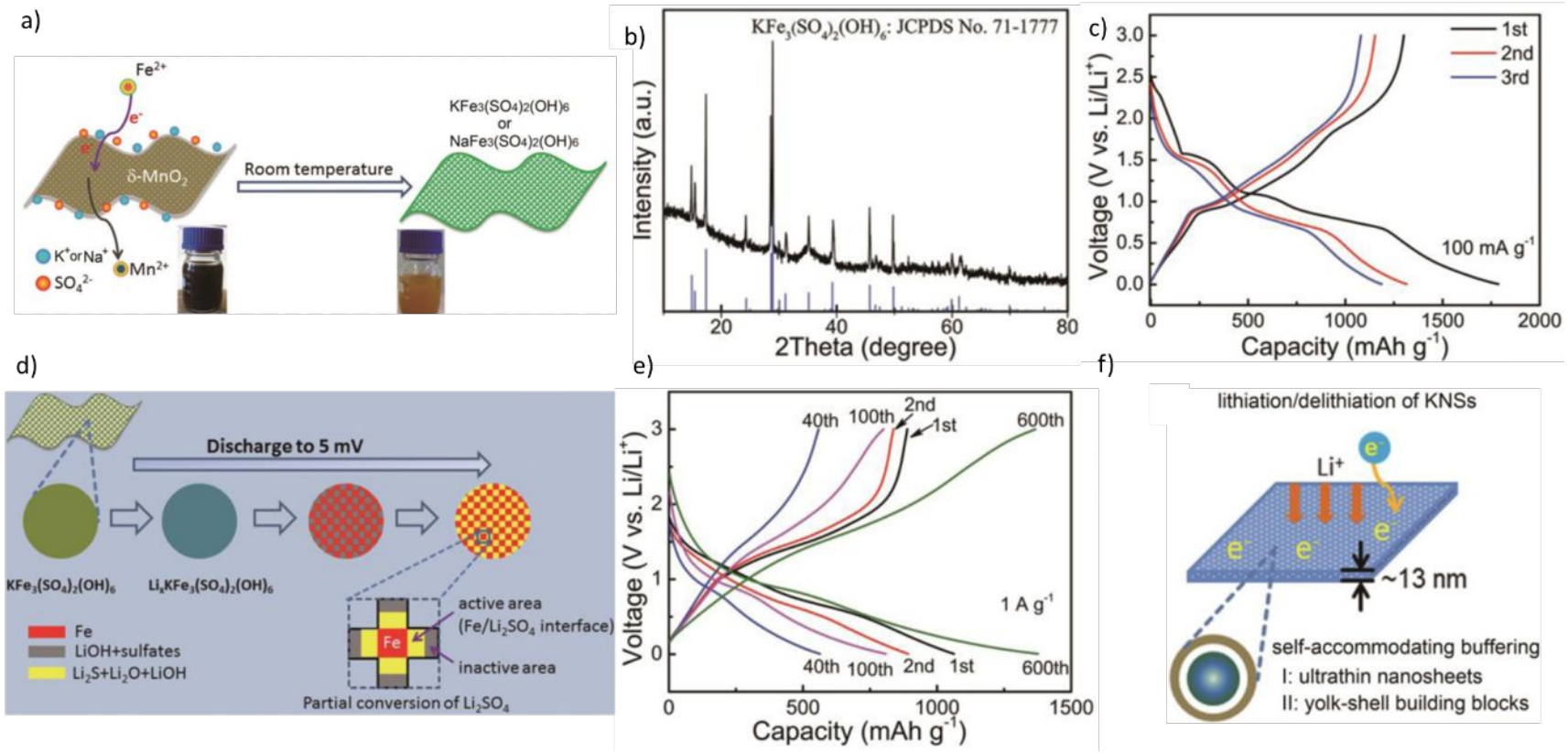


**Figure 9**. (a) Schematic illustrations of $KFe_3(SO_4)_2(OH)_6$ jarosite nanosheets synthesized by a template-assisted redox coprecipitation method at room temperature. (b) XRD pattern of jarosite nanosheet matched with reference pattern corresponding to ICSD No. 71-1777. (c) Galvanostatic (Dis)charge profiles of jarosite acquired between 0.005 and 3.0 V at a high current rate of 100 $mAg^{-1}$. (d) Phase evolution during the initial discharge process for jarosite electrode from open circuit potential to 5 mV. (e) (Dis)charge curves of jarosite over prolonged cycling at a slower current rate of 1 $Ag^{-1}$. (f) Schematic illustration of the yolk-shell architecture of jarosite nanosheet believed to impart enhanced cycling stability. Reproduced with permission.[108] Copyright 2015, American Chemical Society.

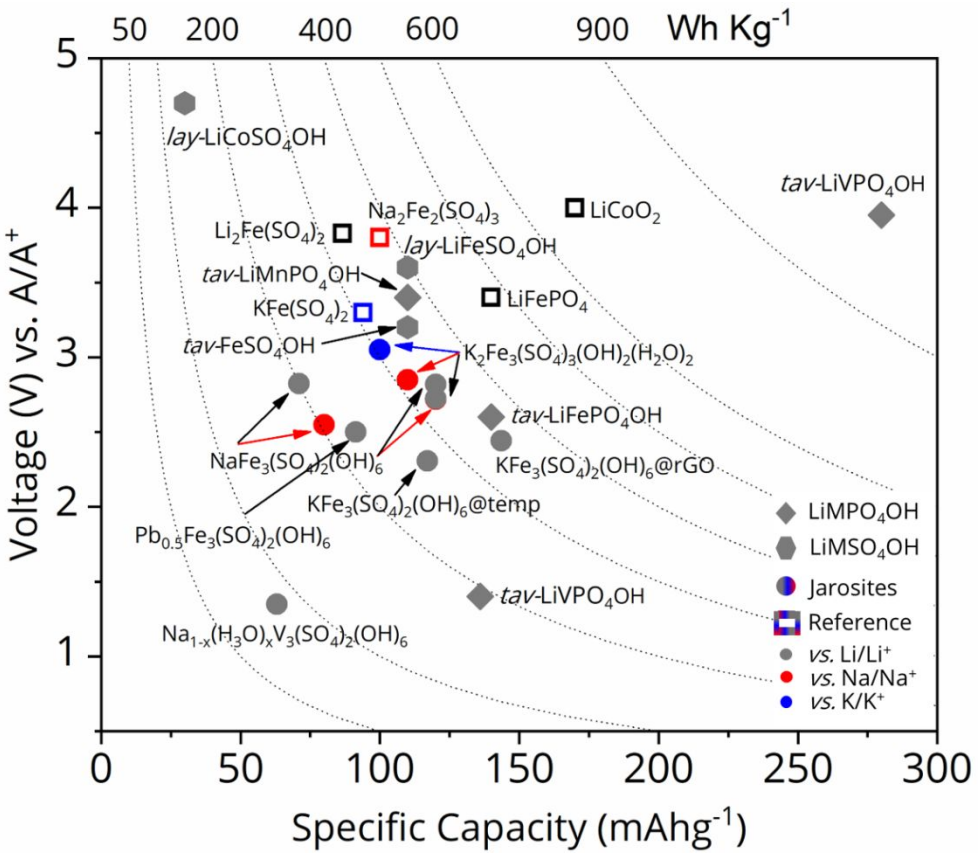


**Figure 10**. Comparative performance of various hydroxy-based cathodes (namely hydroxyphosphates, hydroxysulfates and jarosites) along with selected state-of-the-art cathodes ($LiCoO_2$, $LiFePO_4$ etc.) are summarised emphasizing their operating voltage, specific capacity and energy density (dashed lines).

**Dr. Prabeer BARPANDA,**
Associate Professor
Materials Research Center,
Indian Institute of Science,
Bangalore- 560012, India.
http://www.prabeer.org

April 21st, 2021

Dear Editor,
*Physical Chemistry Chemical Physics*,
RSC Publications.

With regards, we would like to submit a perspective article "*An overview of hydroxy-based polyanionic cathode insertion materials for metal-ion batteries*" authored by S. Singh, S. Lochab, L. Sharma, V. Pralong and myself, for your consideration to publish in *Physical Chemistry Chemical Physics*. We have prepared this article following your kind invitation last year.

High energy density polyanionic cathode materials form the cornerstone for next generation rechargeable batteries. They exhibit rich diversity in their structure, electrochemistry and various physical properties. One such sub-class of polyanionic material family is "hydroxy-based insertion materials", having $OH^-$ moieties. The current article focuses on hydroxy-containing cathode materials with three broad types: (i) hydroxyphosphates, (ii) hydroxysulfates and (iii) (non)jarosites. The presence of one or more $OH^-$ units render structural diversity and diverse magnetic, electronic and electrochemical properties in these hydroxy-based cathode materials.

We strongly believe this article will attract the attention of battery as well as materials community to further explore hydroxy-based battery electrode materials. This is the first dedicated review on hydroxy-based insertion materials. We declare the content is original and is not under consideration elsewhere. All authors comply by the ethical standards of RSC Publications and have given their consent for submission. Once again, we sincerely thank you for your kind invitation and consideration of our manuscript for publication in *Physical Chemistry Chemical Physics*. We look forward to your kind response.

Sincerely yours,

Prabeer Barpanda

Prabeer Barpanda

**Materials Research Center, Indian Institute of Science, Bangalore 560012, India.**
**Phone**: +91 (0)80 2293 2783 **Fax**: +91 (0)80 2360 7316 **Cell**: +91 94495 20638
**E-mail**: prabeer@iisc.ac.in **Homepage**: http://www.prabeer.org